Delft University of Technology

Geometric effects on impact mitigation in architected auxetic metamaterials

Gärtner, T.; van den Boom, S. J.; Weerheijm, J.; Sluys, L. J.

Important note
To cite this publication, please use the final published version (if applicable).
Please check the document version above.

Research paper

Geometric effects on impact mitigation in architected auxetic metamaterials

T. Gärtner [a,b,*], S.J. van den Boom [b], J. Weerheijm [a], L.J. Sluys [a]

[a] *Faculty of Civil Engineering and Geosciences, Delft University of Technology, Postbus 5048, 2600 GA Delft, The Netherlands*
[b] *Netherlands Institute for Applied Scientific Research (TNO), Postbus 480, 2501 CL Den Haag, The Netherlands*

ARTICLE INFO

ABSTRACT

Lightweight materials used for impact mitigation must be able to resist impact and absorb the maximum amount of energy from the impactor. Auxetic materials have the potential to achieve high resistance by drawing material into the impact zone and providing higher indentation and shear resistance. However, these materials must be artificially designed, and the large deformation dynamic effects of the created structures must be taken into consideration when deciding on a protection concept. Despite their promise, little attention has been given to understanding the working mechanisms of high-rate and finite deformation effects of architected auxetic lattice structures. This study compares the static and dynamic elastic properties of different auxetic structures with a honeycomb structure, a typical non-auxetic lattice, at equivalent mass and stiffness levels. In this study, we limit the investigation to elastic material behavior and do not consider contact between the beams of the lattices. It is demonstrated that the equivalent static and dynamic properties of individual lattices at an undeformed state are insufficient to explain the variations observed in impact situations. In particular, the initial Poisson's ratio does not determine the ability of a structure to resist impact. To gain a thorough comprehension of the overall behavior of these structures during localized, high rate compression, the evolution of the elastic tangent properties under compression and shear deformation was monitored, leading to a more profound understanding. Observations made in one configuration of stiffness and mass are replicated and analyzed in related configurations.

1. Introduction

Impact events occur on various types of structures, ranging from roofs damaged by hailstorms (Saini and Shafei, 2019) to civil structures exposed to accidents, such as a car hitting a bridge pillar (Pan et al., 2018). Detonation debris hitting personal protective equipment (see e.g. Crouch, 2019) or satellites in orbit threatened by micrometeorites and space debris (Pardini and Anselmo, 1999) are examples of high impact velocity scenarios that occur in a military or space context. In the quest for better mitigation of these impacts, auxetic[1] materials – materials with a negative Poisson's ratio – exhibit several beneficial properties, such as higher indentation resistance (Argatov et al., 2012) and shear resistance (Choi and Lakes, 1992), as well as increased fracture toughness (Choi and Lakes, 1996) and energy absorption (Jiang and Hu, 2017). These properties are promising in the quest for lightweight materials for impact protection.

The differences in deformation behavior between non-auxetic and auxetic materials are visualized in Fig. 1.1. On the left, the lateral expansion is sketched during compression, as expected for materials

with a positive Poisson's ratio. The right side of the figure shows the lateral contraction after compression, as indicated by a negative Poisson's ratio. This lateral contraction leads to a densification of the material at the point of impact. In addition to the properties mentioned above, this promises additional impact resistance.

Auxetic materials are rarely found in nature (e.g. cow teat skin Lees et al., 1991 or crystalline silica Keskar and Chelikowsky, 1992), but they can be artificially constructed through careful design, as shown in various reviews (Ren et al., 2018; Zhang et al., 2020; Wang et al., 2020; Bohara et al., 2023). As the reviews show, the approach to designing auxetic metamaterials is well understood, but limited to static problems, and there are myriad types of auxetic architectures (see also Álvarez Elipe and Díaz Lantada, 2012). Since the understanding of internal deformation patterns in dynamic environments and the resulting implications for the use of auxetic metamaterials in protective layers is limited and mostly based on macroscale investigations with little insight into the workings at mesoscale, there is a need for a better understanding of the dynamic properties of these structures. Tatlıer

---

[1] the term was coined by Evans et al. (1991) from the Greek `auxetos` "that may be increased".
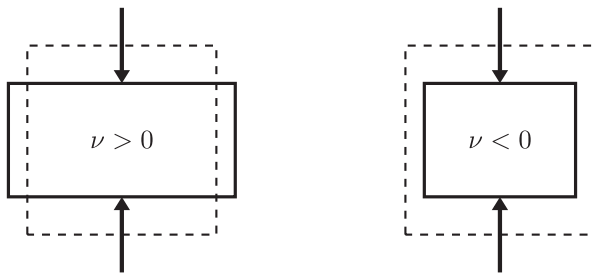
Fig. 1.1. Positive Poisson's ratio materials ($\nu > 0$) and negative Poisson's ratio or auxetic materials ($\nu < 0$) under compression.
Source: Adapted from Lim (2015).

(a)   (b)

Fig. 2.1. Chiral architecture. (a) shows the design and geometric parameters, (b) illustrates uniaxial compression.

(2022) compares different auxetic structures with comparable weight in crushing events without discussing the equivalent properties of the unit cells or their internal deformation mechanism. Even when the deformation mechanisms are described, the authors focus on one type of lattice only (e.g. Zhao et al., 2018 describe the dynamic performance of arrowhead structures, Mercer et al., 2022 investigate different re-entrant lattices).

As can be seen from the reviews on the subject, there are many possibilities for designing auxetic metamaterials. The linear, static properties of all these structures in the undeformed state are well understood (Ren et al., 2018; Wang et al., 2020). In Reda et al. (2018), the interaction between anisotropy and finite strains up to 10% on the resulting static properties is studied together with the phase velocities of acoustic waves propagating through the lattice for Euler–Bernoulli beam structures with negligible bending stiffness. In impact scenarios, however, larger deformations (up to full densification) are expected with nonlinear waves propagating through the lattice structure. The dynamic properties of different auxetics – and the influence on impact mitigation – are mainly reported phenomenologically for singular auxetic architectures without any comparison of different architectures under similar circumstances (see among others Alomarah et al., 2020; Chen et al., 2021; Gálvez Díaz-Rubio et al., 2021).

This study contributes a first step in addressing the lack of understanding of the deformation behavior of (auxetic) architected materials under high-rate localized compression by comparing the geometrically nonlinear static and dynamic properties of different architectures in a purely elastic environment. Our focus is on two-dimensional structures in order to identify the interdependencies between the lattice architecture and the resulting dynamic behavior. We compare a set of different architectures based on the underlying mechanisms that produce auxeticity, all designed to exhibit the same linear-elastic properties and mass density. The study is carried out for nonlinear and dynamic problems and offers explanations for the observed differences. The different auxetic architectures are studied using a custom finite element (FE) implementation of nonlinear Timoshenko beams following (Simo and Vu-Quoc, 1986; Crisfield and Jelenić, 1999) for greater flexibility and computational performance. For the dynamic simulations a predictor–corrector scheme with step-size control is implemented. In this study material nonlinearities and contact between the bars are ignored.

The paper is structured as follows: In Section 2 an overview of the possibilities to generate auxeticity in architected materials is given. Then, in Section 3, the numerical framework and its mechanical background are discussed. In Section 4, linear, static studies are performed on unit cells to find comparable configurations of different architectures. It is shown how these linear properties change when entering the nonlinear regime. The resulting dynamic effects are reported in a localized impact test including a study on strain rate effects. In Section 5, the performance implications of the different architectural approaches are discussed. Finally, conclusions are drawn, and limitations of this study are presented.
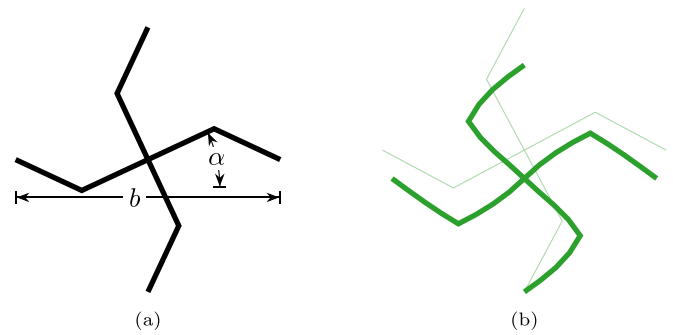
2. Auxetic architectures

2.1. Design options

The auxetic effect is based on the lateral inward movement of parts of the structure under uniaxial compression. This inward movement can be explained by two main mechanisms: rotation and inward folding.[2] In the following, different unit cell architectures and the corresponding design parameters will be explained. A unit cell, in the context of this publication, is the smallest part of a lattice that can be copied and connected to create the entire lattice.

The first class of auxetic architectures is constituted by those that derive their negative Poisson's ratio from rotation at the joints. These so-called *chiral* structures generate a rotating effect with circularly oriented beams, thus inducing rotation under compression. The chiral structure considered is the model introduced by Smith et al. (2000), under a different name, to describe the behavior of auxetic foams. In Bahaloo and Li (2019), the effects of geometrical parameters on the linear effective properties of the structure are described. A schematic of the chiral architecture is shown in Fig. 2.1(a) and its auxetic mechanism is illustrated in Fig. 2.1(b). For the design of this architecture, it should be noted that due to the linear elasticity model on the material level, structures with geometric similitude exhibit the same equivalent properties. Thus, the width b and the thickness of the bars d are not chosen as independent parameters but rather the ratio $t = d/l_c$, with $l_c = 0.5b/\cos\alpha$ as the length of a central bar. Next to this ratio, the angle of the bars α is a variable measure. The colors in the mentioned and the following figures represent the same architecture throughout the manuscript in all illustrations and graphs.

Taking four chiral unit cells and mirroring every other cell creates an *antichiral* structure, where a single unit cell consists of four rotational centers with alternating directions. The antichiral architecture is presented in Fig. 2.2(a) with its deformation mechanism in Fig. 2.2(b).

The second class of architectures is composed of lattice structures that fold at the joints. In order to create an auxetic effect, this class consists of non-convex polygons, i.e. polygons with a reflex angle ($\theta > 180°$). The auxetic effect is caused by the non-convexity of the re-entrant structures, which causes them to fold laterally inwards under compression. The most prominent example of this is a *re-entrant honeycomb* (see among others Gibson et al., 1997). The parameters of this architecture are shown in Fig. 2.3(a) and the working mechanism is illustrated in Fig. 2.3(b). Again, due to geometric similitude the

---

[2] Körner and Liebold-Ribeiro (2015) argue that these two effects can be further reduced to a single mechanism, namely rotation. They describe a workflow to generate arbitrary auxetic structures based on eigenmode analysis. To explain the folding mechanism, they consider out-of-plane modes and recover the rotation mechanism by projecting the eigenmodes onto a plane. This results in beam rotation as opposed to joint rotation.
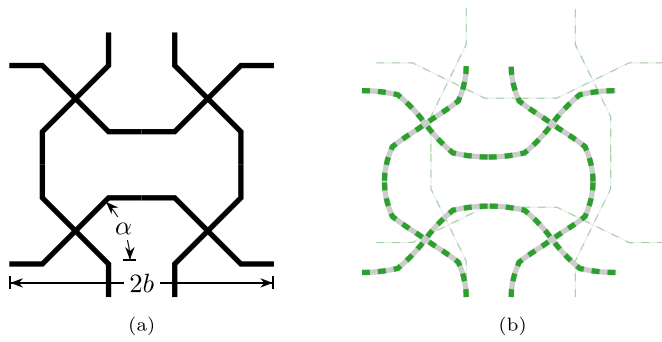
(a)

(b)

Fig. 2.2. Antichiral architecture. (a) shows the design and geometric parameters, (b) illustrates uniaxial compression.
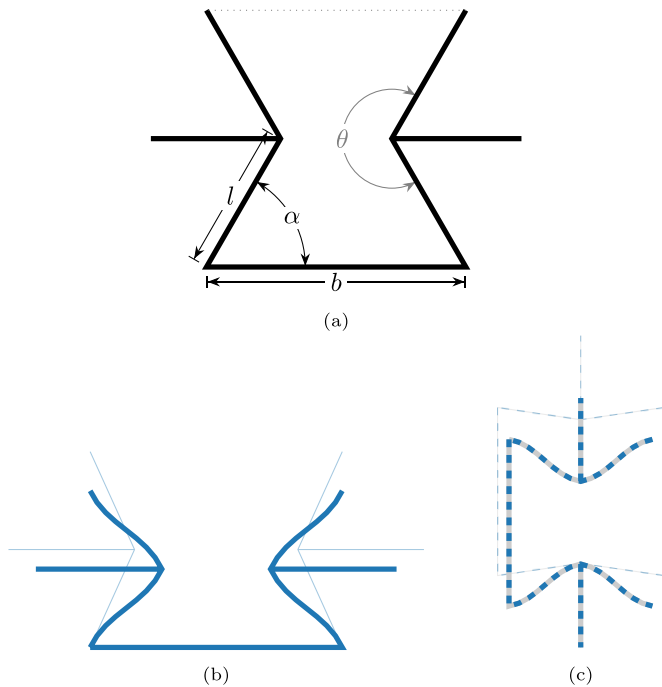

(a)

(b)

(c)

Fig. 2.3. Re-entrant honeycomb architecture. (a) shows the design and geometric parameters, uniaxial compression is illustrated in (b) for 0° orientation and in (c) for 90° orientation.

(a)

(b)

(c)

Fig. 2.4. Arrowhead architecture. (a) shows the design and geometric parameters, uniaxial compression is illustrated in (b) for 0° orientation and in (c) for 90° orientation.

Table 2.1
Range of properties for different architectures.

Architecture	α	t	r	β	design constraint
re-entrant	(20°, 85°)	(0.01, 0.1)	$\left(\frac{1}{3}, \frac{4}{3}\right)$	––	$r < \frac{1}{2\cos\alpha}$
arrowhead	(5°, 45°)	(0.01, 0.1)	––	(50°, 80°)	$3\tan\alpha < \tan\beta$
chiral	(5°, 60°)	(0.01, 0.1)	––	––	
antichiral	(5°, 60°)	(0.01, 0.1)	––	––	
honeycomb	(95°, 145°)	(0.01, 0.1)	$\left(\frac{1}{3}, \frac{4}{3}\right)$	––	

properties do not change with absolute scale, instead of the lengths, l and b, individually their ratio $r = \frac{l}{b}$ is taken as design variable and instead the thickness of a single beam d, the thickness scaled to the base length $t = \frac{d}{b}$ is taken as variable. Finally, the angle between the base and the angled beams α is added to the set of variables for this architecture. Since the properties of this architecture are not invariant to the orientation, this architecture will also be investigated rotated by 90°. The corresponding deformation mechanism is shown in Fig. 2.3(c).

While the re-entrant structure has two opposing folds, another architecture with two folds in the same direction is the *arrowhead* structure. This commonly investigated auxetic structure was originally the result of a topology optimization for negative Poisson's ratio (Larsen et al., 1997). The architecture is visualized in Fig. 2.4(a) along with its parameters and the working mechanism shown in Fig. 2.4(b). In this structure, the beam thickness d is scaled with the height of the unit cell $t = \frac{d}{h}$. The three variables, that determine the properties of this structure are the two angles of the longer beam β as well as the shorter beam α and the height h. As with the re-entrant honeycomb structure, this architecture is also studied rotated by 90°. The corresponding deformation mechanism is shown in Fig. 2.4(c).
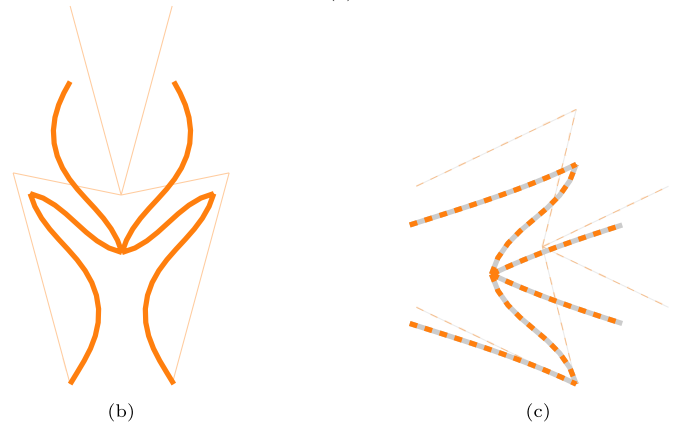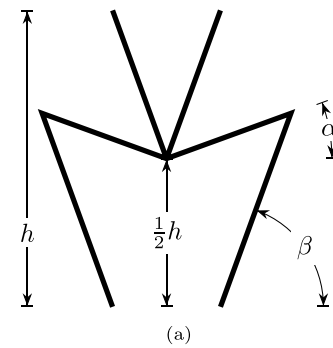
To allow for a comparison of the different architectures, a non-auxetic architecture is also included as a reference. Since the *normal honeycomb* is based on the same architecture as the re-entrant honeycomb, it is included in the study. Due to this similarity, its properties are determined by the same geometry factors as the re-entrant honeycombs, namely the ratio between the beam lengths $r = \frac{l}{b}$, the ratio between the thickness and the base length $t = \frac{d}{b}$ and the angle between the base beams α. Similar to the argumentation in the re-entrant architecture, investigations are also conducted with the structures rotated by 90°. The general configuration is depicted in Fig. 2.5(a), with the deformation mechanisms are shown in Figs. 2.5(b) and 2.5(c) for the 0° and 90° orientation respectively.

2.2. Design selection

The parameters of all the selected architectures are tuned so that all the lattices in the undeformed configuration have the same Young's modulus in the vertical direction and the same relative density. The following is a brief explanation of the procedure for metamaterials with a density relative to the constituent material

$$\rho_{\text{rel}}^{\star} = \frac{\rho}{\rho_{\text{mat}}} = 0.1$$

and an equivalent Young's modulus $E_y^{\star} = 300\,\text{MPa}$, where $(\cdot)^{\star}$ represents target properties. For all investigations, the base material of the

Table 2.2

Resulting properties and unit cells of the investigated architectures with target properties $E_y^\star = 300\,\text{MPa}, \rho_{\text{rel}}^\star = 0.1$.

| Geometry	t	α [°]	β [°]	r	ρ_{rel}	E_y [MPa]	E_x [MPa]	ν_{yx}	ν_{xy}	G_{xy} [MPa]	G_{yx} [MPa]
re-entrant	0.035	65.62	–	0.43	0.100	297	273	−1.00	−0.92	8	8
re-entrant (90°)	0.046	81.67	–	0.50	0.100	297	2,937	−0.26	−2.60	15	15
arrowhead	0.021	11.60	74.90	–	0.100	296	468	−0.73	−1.16	924	924
arrowhead (90°)	0.030	13.81	64.34	–	0.100	295	80	−1.85	−0.50	1,583	1,583
chiral	0.078	28.11	–	–	0.100	299	299	−0.38	−0.38	53	19
antichiral	0.085	26.09	–	–	0.100	299	299	−0.69	−0.69	10	10
honeycomb	0.094	119.69	–	1.14	0.100	299	243	1.08	0.88	87	87
honeycomb (90°)	0.096	125.63	–	1.17	0.100	299	187	1.24	0.77	100	100

Fig. 2.5. Honeycomb architecture. (a) shows the design and geometric parameters, uniaxial compression is illustrated in (b) for 0° orientation and in (c) for 90° orientation.

structures is set as a generic metal with $E_{\text{mat}} = 210\,\text{GPa}$, $\nu_{\text{mat}} = 0.3$, and $\rho_{\text{mat}} = 7850\,\text{kg}\,\text{m}^{-3}$.

Since this study assumes linear elastic material behavior at the microscale, structures with geometric similitude can be assumed to have identical properties. Thus, as explained above, the thickness t of the beams related to the primary length of the unit cell as well as the ratio between the beam lengths r are taken as free variables. All free variables are tuned within their ranges and conditions reported in Table 2.1 to ensure realistic structures. The ranges and conditions are explained in more detail in Appendix A. Given these design ranges, the individual structures are subsequently tuned to exhibit properties as close to the targets as possible. The resulting properties as well as visualizations of the corresponding unit cells are shown in Table 2.2. Details of the tuning process and results for different target lattice properties are shown in Appendix A.

3. Numerical framework

The aforementioned lattice structures are implemented as nonlinear Timoshenko beams, also known as Simo–Reissner beams (Reissner, 1981; Simo, 1985) or special Cosserat rods (see also Antman, 2005;
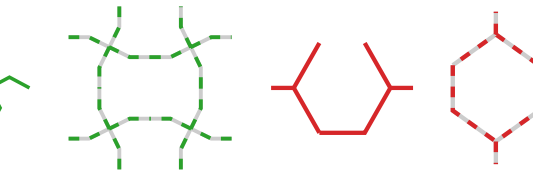
Eugster, 2015). The implementation for this work is carried out using the JIVE-Framework (Dynaflow Research Group, 2021).

A nonlinear Timoshenko beam can be described by its centerline and the orientation of its cross-section along the length of the beam. This results in a mapping from a one-dimensional length space to a six-dimensional configuration space. In this six-dimensional configuration space, derivatives can be calculated to obtain a six-dimensional strain space for the beam. For details, see Antman (2005) and Eugster (2015). The relationship between the beam-type strains and the beam-type stresses is assumed to be linear elastic for this work.

For the FE discretization, this study follows the approach of Simo and Vu-Quoc (1986) for the determination of the stiffness matrices and the resulting nodal forces. Linear Lagrangian shape functions are used to interpolate the position vectors, with reduced integration to avoid shear-locking phenomena. The orientation matrices are interpolated using spherical interpolation as suggested by Crisfield and Jelenić (1999). Derivations and detailed explanations can be found in the referenced literature.

The time integration for the dynamic simulations is performed by a pairing of an explicit and an implicit Euler scheme in a predictor–corrector fashion in order to ensure fast computation times for the small time steps required for the high-speed impact computations while maintaining accuracy. For this purpose, the system of second-order differential equations is transformed into a system of first-order differential equations by introducing the node velocities as additional state variables. To ensure the reliability of the simulations, step-size control is employed using a Milne-device (Milne, 1926) error estimator. The orientation matrices, which belong to the special orthogonal group SO(3), are integrated using an exponential integrator (see e.g. Munthe-Kaas, 2015).

3.1. Tangent property computation

The linear equivalent properties of a unit cell need to be computed for simple deformation modes. In order to do so, PBCs were implemented. Since the investigated architectures do not possess nodes in the corners, *ghost* nodes have been introduced for the application of the PBCs. The implementation of this procedure is explained in Appendix B.1.

In order to determine the equivalent elastic properties in a deformed state, a simple approach using finite differences was chosen. The incremental displacement gradient δH is related to incremental Piola–Kirchhoff stresses δP by tangent stiffness tensor $\mathbb{C}^4$

$$\delta P = \mathbb{C}^4 : \delta H. \tag{3.1}$$

In order to estimate the elastic properties at a fixed deformation in a first step, the displacement gradient at this deformation H_o is recorded.

Then in a next step, this displacement gradient is perturbed in one direction

$$\boldsymbol{H}^{ij\pm} = \boldsymbol{H}_\circ \pm 0.5 \times 10^{-9} \begin{bmatrix} \delta_{i1}\delta_{j1} & \delta_{i1}\delta_{j2} \\ \delta_{i2}\delta_{j1} & \delta_{i2}\delta_{j2} \end{bmatrix} \quad i,j \in [1,2] \tag{3.2}$$

with the Kronecker delta δ_{kl}. The corresponding 1st Piola–Kirchhoff stress tensors $\boldsymbol{P}^{ij\pm}, i,j \in [1,2]$ are then recorded. For all directions, corresponding tangent properties are first computed by addition of the recorded values

$$\begin{aligned} \Delta\boldsymbol{H}^{ij} &= \boldsymbol{H}^{ij+} - \boldsymbol{H}^{ij-} \\ \Delta\boldsymbol{P}^{ij} &= \boldsymbol{P}^{ij+} - \boldsymbol{P}^{ij-} \end{aligned} \quad i,j \in [1,2]. \tag{3.3}$$

Then the coefficients of the tangent stiffness tensor are determined by dividing the stresses by the corresponding strains:

$$c_{ijkl} = \frac{\Delta P_{ij}^{kl}}{\Delta H_{kl}^{kl}}. \tag{3.4}$$

Finally, using the inverse of the stiffness tensor $\mathbb{C}^4$, the compliance tensor $\mathbb{S}^4$, the equivalent tangent Young's modulus is calculated by rearranging the equation

$$\begin{bmatrix} \delta H_{11} & 0 \\ 0 & \delta H_{22} \end{bmatrix} = \mathbb{S}^4 : \begin{bmatrix} \delta P_{11} & \delta P_{12} \\ \delta P_{21} & 0 \end{bmatrix} \tag{3.5}$$

for

$$\delta H_{11} = \frac{1}{E_{11}} \delta P_{11}. \tag{3.6}$$

The Poisson's ratio is then found by further rearrangements leading to

$$\delta H_{22} = -\nu_{12}\delta H_{11}. \tag{3.7}$$

Similar procedures are employed to determine the tangent properties E_{22} and ν_{21}.

The constrained moduli M_{11}, M_{22} and shear moduli G_{12}, G_{21} are determined by rearrangements of the equation

$$\begin{bmatrix} \delta H_{11} & 0 \\ 0 & 0 \end{bmatrix} = \mathbb{S}^4 : \begin{bmatrix} \delta P_{11} & \delta P_{12} \\ \delta P_{21} & \delta P_{22} \end{bmatrix} \tag{3.8}$$

for

$$\delta H_{11} = \frac{1}{M_{11}} \delta P_{11}. \tag{3.9}$$

Again, identical procedures are employed to determine G_{12}, G_{21}, and M_{22}. Details are found in Appendix B.2.

4. Numerical results

Using the methods described in Section 3 and the unit cells derived from the architectures as described in Section 2, the changes in the properties of unit cells subjected to large deformations are discussed below. First, the equivalent Young's modulus and Poisson's ratio as static properties are presented, followed by an overview of the equivalent lateral to the impact (*x*-direction) pressure and shear wave speeds as well as the longitudinal to the impact (*y*-direction) pressure wave speeds as dynamic properties of the different architectures. Finally, the behavior of the different architectures under high strain rate and localized compression is examined and discussed.
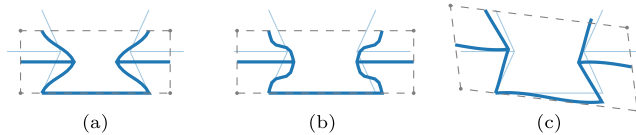

Fig. 4.1. (a) uniaxial compression (Eq. (4.1)), (b) planar compression (Eq. (4.2)) and (c) pure shear deformation (Eq. (4.3)) of the re-entrant unit cell using the PBCs as in Fig. B.1.
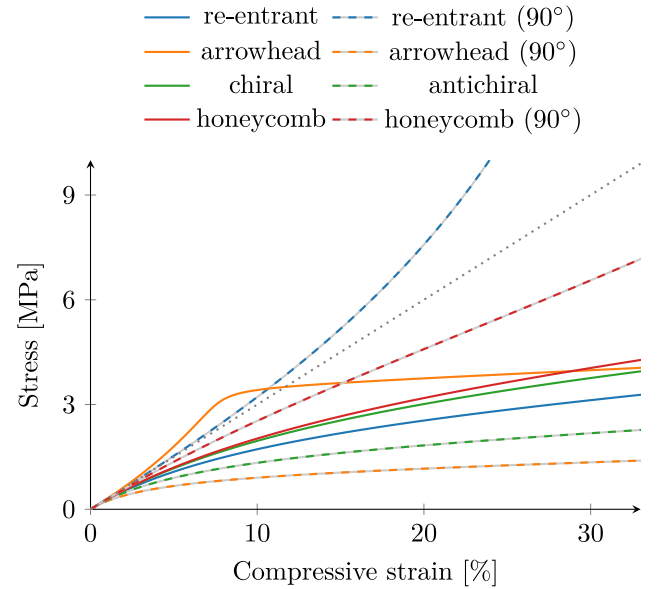

Fig. 4.2. Stress–strain curves in uniaxial (unconstrained) compression for different architectures.

4.1. Static properties of the architectures

The evolution of the initial static properties of each architecture, reported in Table 2.2, is investigated with the procedures described in Section 3.1 applied to single unit cells. Structures that maintain high stiffness over a wide range of deformations are expected to have higher resistance in an impact scenario, as the decelerating forces on the impactor are high over the range of deformation to be expected during impact. To estimate this, three types of deformation are considered: (a) unconstrained uniaxial compression (in the following called uniaxial), (b) constrained uniaxial (in the following called planar) compression, and (c) pure shear deformation, as visualized in Fig. 4.1.

The architectures are first exposed to uniaxial compression. This is done by applying the displacement gradients

$$\boldsymbol{H} = k \begin{bmatrix} \bullet & 0 \\ 0 & -1 \end{bmatrix} \quad k \in [0, 0.33], \tag{4.1}$$

where $\bullet$ denotes no constraint. This deformation mode is illustrated in Fig. 4.1a. At each deformation step the corresponding equivalent elastic tangent properties are recorded as well as the current stresses and strains at the four boundaries. Since contact and interpenetration of different beams, which is not modeled by the numerical framework, occur at later stages of deformation, in the following only compression up to $k = 33\%$ will be discussed.

In the stress–strain curve (Fig. 4.2), it is shown that all but two structures show a reduced stiffness under uniaxial compression. The *rotated* re-entrant honeycomb structure (depicted by the dashed blue line) is the only structure that keeps stiffening. This effect is due to the fact, that the folding mechanism aligns the beams in vertical direction, promoting axial loading over bending in uniaxial compression. The same explanation holds for the initial stiffening of the arrowhead structure. However, at approximately 6.5% compression the beams start to buckle, leading to a transition from axial loading to loading in bending and thus an overall weakening at larger deformations. These effects are depicted as well in Fig. 4.3a, where the normalized equivalent Young's modulus E_y is plotted against the compressive strain. In this figure some relevant deformation patterns of the architectures are visualized as well. The buckling of the arrowhead structure (depicted in solid orange) can be seen at the plotted deformation patterns at 6% and at 7% compression. Prior to buckling the alignment of the beams is in vertical
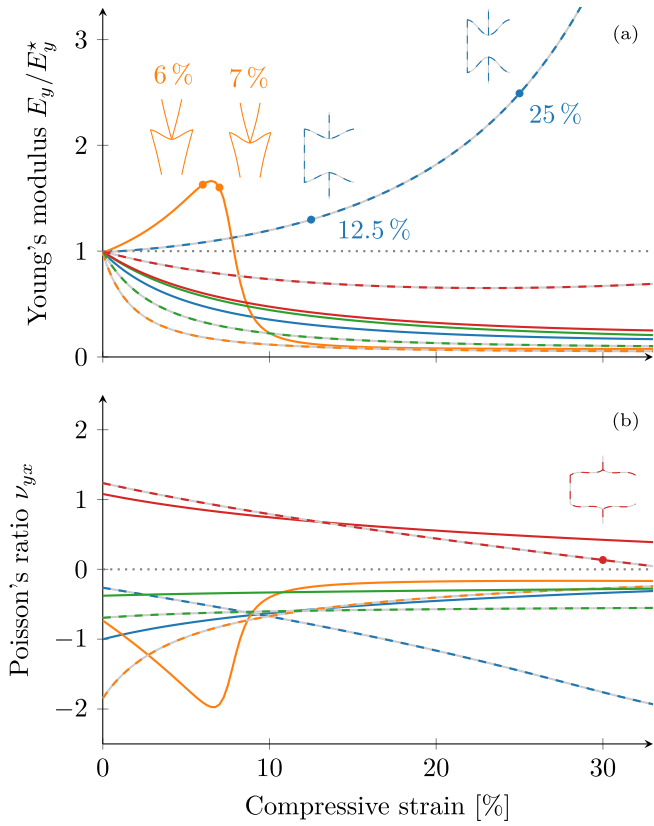
Fig. 4.3. Change of properties under uniaxial (unconstrained) compression for different architectures, namely (a) the normalized (unconstrained) Young's modulus E_y and (b) the Poisson's ratio ν_{yx}.

direction, leading to more axial loading. After buckling, the beams are loaded in bending again. Similarly, the vertical alignment of the beams in the rotated re-entrant honeycomb structure is clearly visible in the deformation sketches in Fig. 4.3a at 12.5 % and 25 %. Additionally, in the lower graph Fig. 4.3b, the Poisson's ratio ν_{yx} is plotted against compression. Structures with a reduced stiffness also exhibit a decrease in involvement of lateral material in larger patches, i.e. a Poisson's ratio developing towards zero. This results in auxetic architectures exhibiting a less pronounced negative Poisson's ratio, thus reducing the effect of lateral material involvement. Noteworthy is the fact, that the rotated regular honeycomb structure, upon compression, resembles the rotated re-entrant honeycomb structure. This is visualized in the deformation pattern at 30 %, and supported by the approximately linear decrease of the Poisson's ratio, leading to a change from non-auxetic to auxetic behavior at high (> 33 %) compression.

During impact, lateral material is confining the lateral displacement of the impacted lattice, thus constrained uniaxial or planar compression resembles an impact scenario better. For the assessment of the impact performance of metamaterials it is therefore valuable to also consider planar compression. This planar compression is described by the displacement gradients

$$\boldsymbol{H} = k \begin{bmatrix} 0 & 0 \\ 0 & -1 \end{bmatrix} \quad k \in [0, 0.33]. \tag{4.2}$$

This deformation mode is illustrated in Fig. 4.1b. In Fig. 4.4 the corresponding stress–strain curves are plotted. It should be noted, that the stresses are much higher compared with the stresses in uniaxial compression (in Fig. 4.2). In planar compression only the rotated re-entrant honeycomb structure exhibits stiffening behavior. The regular honeycomb and arrowhead architectures both display reduced stiffness
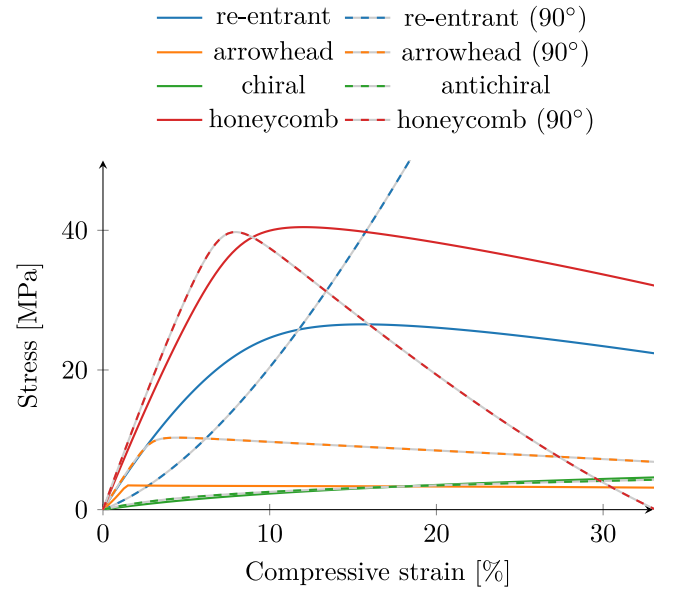
Fig. 4.4. Stress–strain curves in planar (constrained) compression for different architectures.
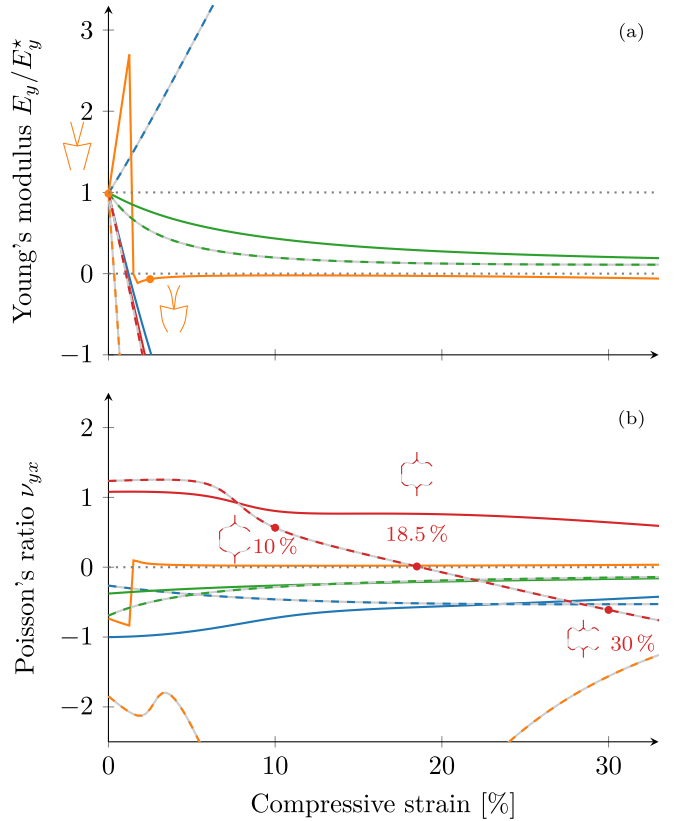
Fig. 4.5. Change of vertical properties in planar (constrained) compression for different architectures, namely (a) the normalized (unconstrained) Young's modulus E_y and (b) the Poisson's ratio ν_{yx}.

leading to snap-through, resulting in negative slopes of the stress–strain curve following substantial planar compression. An illustration of the corresponding deformed structures is provided in Fig. 4.5 for the rotated honeycomb unit cell. This behavior is also observed in the re-entrant honeycomb unit cell. The normalized Young's modulus E_y plotted against the deformation as done in Fig. 4.5a shows a similar

Fig. 4.6. Stress–strain curves in pure shear for different architectures.

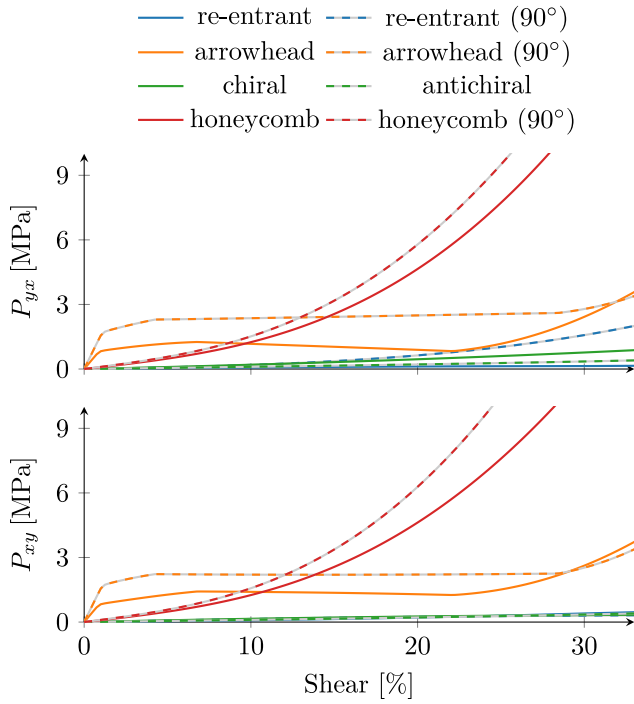**Fig. 4.7.** Change of vertical properties under pure shear deformation for different architectures, namely (a) the normalized Young's modulus E_y and (b) the Poisson's ratio ν_{yx}.

Fig. 4.8. Pure shear deformation pattern of arrowhead structures.

behavior. It should be noted here, that the Young's modulus as proxy for the *un*constrained uniaxial tangent stiffness in Fig. 4.5a is not equal to the derivative of the constrained stress–strain curve in Fig. 4.4. The stiffness for all but the (anti-)chiral and the rotated re-entrant honeycomb architecture become negative, resulting in loss of resistance against unconstrained compression. In the lower graph, Fig. 4.5b, the Poisson's ratio ν_{yx} is plotted against the compressive strain. Here, the rotated regular honeycomb's transition from non-auxetic to auxetic behavior is even more pronounced than for uniaxial compression and can be observed around 18.5 % compression. The deformation patterns at 10 % and 30 % planar compression show the transitions from the convex honeycomb shape towards a non-convex shape resembling – like in the uniaxial case – a re-entrant honeycomb structure. Also, the arrowhead structure transfers from auxetic into non-auxetic behavior after buckling (in planar compression at approximately 1.5 %). This buckling is visualized in the deformation patterns at 0 % and 2.5 % planar compression in Fig. 4.5a.

In an impact scenario also significant shear deformation may be expected. The development of different architectures under shear deformation is thus investigated by applying the displacement gradient

$$\boldsymbol{H} = k \begin{bmatrix} 0 & -0.5 \\ -0.5 & 0 \end{bmatrix} \quad k \in [0, 0.33] . \tag{4.3}$$

This deformation mode is illustrated in Fig. 4.1c. In Fig. 4.6, the stress–strain curves for both shear components are shown. In the stress–strain curves, the regular honeycomb structures show the strongest resistance towards shear at higher deformations. The arrowhead structures show a steep decline in shear resistance, as they initially show the highest stresses upon shear deformation, followed by only minor increase in stresses at increasing strains. In Fig. 4.7 the normalized Young's modulus and the Poisson's ratio are plotted against shear deformation. Here, apart from the arrowhead structures, all structures show an increasing Young's modulus. Especially the non-auxetic honeycomb structures show an increase, which is significantly larger compared to the corresponding auxetic structures. The arrowhead structures exhibit three regimes across the range of shear deformation examined. The progressive deformation patterns throughout shear deformation are shown
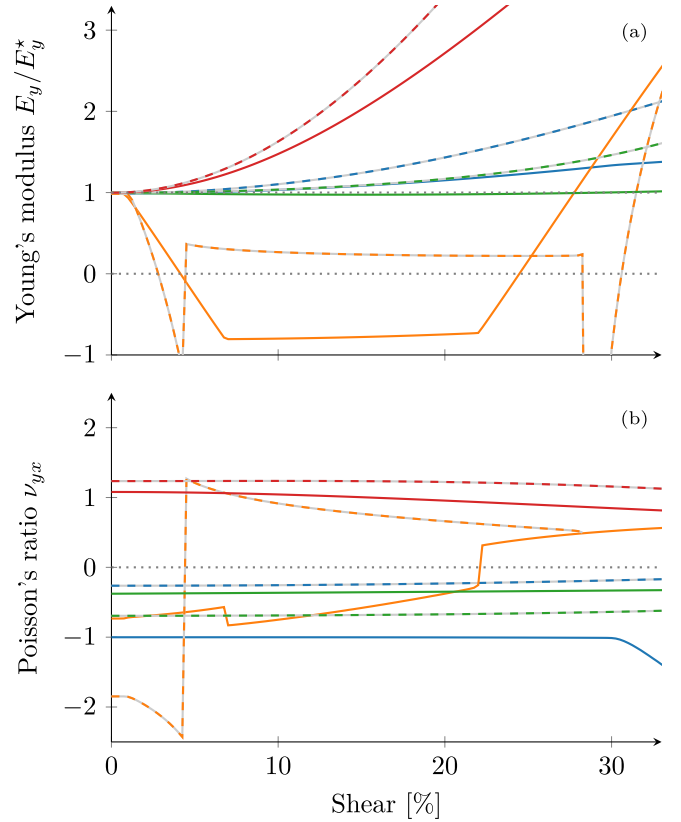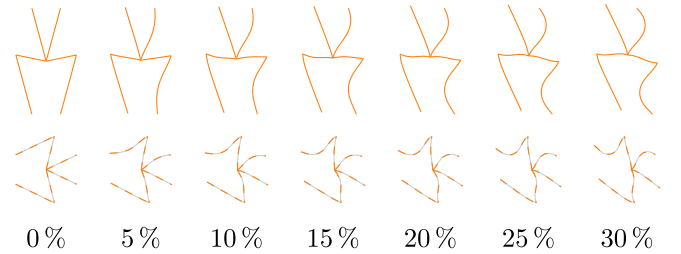
in Fig. 4.8. After a steep initial decline in Young's modulus, an almost constant modulus is seen before the Young's modulus finally starts to increase. These regions in the stiffness properties for the arrowhead architecture are explained by the fact that the two central beams in the unit cell initially form a downwards facing half-wave. Throughout deformation, the amplitude of this half-wave is decreasing, leading to load transfer by bending and pre-stresses even leading to negative Young's moduli, as can be seen in Fig. 4.7a. After some deformation one of the two central beams suddenly shows large deformation, leading to the two central beams resembling a full sine wave with one node of the wave at the central joint. This is occurring at 4 % for the rotated and 7 % for the unrotated variant. Here, further deformation does not change the overall vertical stiffness of the unit cell, as the connecting joint is now resembling the node of the wave. At 28 % for the rotated and 22 % for the unrotated variant the second beam again shows a sudden deformation in such a way, that the two central beams again resemble a (now upwards facing) half-wave. The connecting joint is located on the peak of this half-wave leading again to stiffening, as every displacement of the joint has the resistance of the beams

working against it. Lastly, the Poisson's ratio (as seen in the lower graph Fig. 4.7b almost remains unchanged under shear deformation for all but the arrowhead architectures. The arrowhead architectures again show two jumps in their tangent properties, coinciding with the earlier mentioned configuration changes.

4.2. Dynamic properties of the architectures

In the assessment of the effects of different architectures in impact scenarios, not only the (static) loading resistance, as discussed in Section 4.1, is of importance, but also the behavior of the architectures in dynamic loading is relevant. First measures to assess this dynamic behavior are the pressure wave speed c_{P_x} and shear wave speed c_{S_x} lateral to the impact direction, as well as the pressure wave speed c_{P_y} longitudinal to the direction of impact. They are computed with the following formulae

$$c_{P_x} = \sqrt{\frac{M_x}{\rho}}, \quad c_{S_x} = \sqrt{\frac{G_{yx}}{\rho}}, \quad c_{P_y} = \sqrt{\frac{M_y}{\rho}} \qquad (4.4)$$

where M_x, G_{yx}, and M_y are determined during deformation as described in Section 3.1. The density ρ is updated with the deformation as well. As these wave speeds are calculated for homogenized cells, wave phenomena with wave lengths smaller than the size of each unit cell are not captured in this approach. Considering the development of the wave speeds $c_{P_x}, c_{S_x}, c_{P_y}$ in the three cases described in Section 4.1 – uniaxial compression, planar compression, and pure shear – offers more insight into the behavior of different architectures under dynamic loading conditions. Higher lateral wave speeds lead to a higher involvement of the lateral material, since the stress concentrations move faster to the sides, i.e. the not impacted sections of the patch leading to a better distribution of energy.

In Fig. 4.9 the wave speeds are plotted against uniaxial compression for all eight architectures. In the top graph (Fig. 4.9a), the lateral pressure wave speed c_{P_x} is shown. It can be seen, that in the undeformed state, the rotated re-entrant unit cell has the highest lateral pressure wave speed of the investigated structures with an obvious decline upon compressive deformation. In the middle graph Fig. 4.9b, the lateral shear wave speeds of the different structures and their development under uniaxial compression are shown. It can be seen, that the lateral shear wave speeds, compared to the lateral pressure wave speeds, are significantly smaller for all architectures but the arrowhead ones. In the lower graph Fig. 4.9c, the longitudinal pressure wave speeds c_{P_y} are shown. They show similar behavior to the Young's moduli in impact direction E_y (compare Fig. 4.3a). The differences are due to the constrained modulus M_y in the formula for the wave speed instead of the (unconstrained) Young's modulus E_y as well as in the consideration of the changing density ρ throughout the deformation.

The peaks in the chiral structure wave speeds in both graphs, Figs. 4.9a and 4.9b, as well as in the rotated re-entrant honeycomb structure in the c_{S_x} graph, are caused by instabilities of the pre-stressed beams undergoing small changes in loading direction leading to 'micro'-buckling, during the finite difference determination of the tangent stiffness tensor $\mathbb{C}^4$. This leads to the structure appearing with greatly exaggerated or reduced stiffness around polar points corresponding to the peaks.

Similar behavior of the wave speeds can be seen in Fig. 4.10, where the wave speeds are plotted against planar compressive strains. Compared with the uniaxial case previously discussed, the rotated re-entrant structure also tends to lose some of its lateral pressure wave speed, as can be seen in Fig. 4.10a. This is, however, less pronounced and since all other structures show a substantial decrease, it maintains the highest lateral wave speed. The shear wave speeds in Fig. 4.10b show similarly low levels as in the uniaxial case. The pressure wave speeds in the impact direction are depicted in Fig. 4.10c. The various peaks, that can be seen, again stem from the pre-stress resultants in the singular
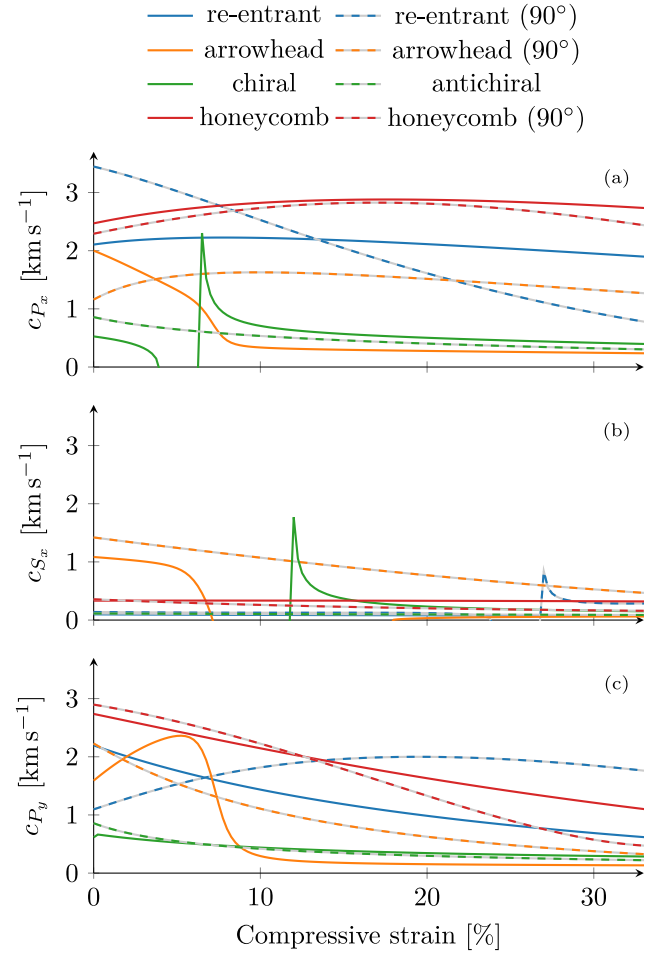

Fig. 4.9. Change of the lateral pressure and shear wave speed under uniaxial compression, (a) shows the lateral pressure wave speed c_{P_x}, (b) shows the lateral shear wave speed c_{S_x}, (c) shows the pressure wave speed in impact direction c_{P_y}.

beam elements at the various stages of compression corresponding instabilities during the finite difference calculation.

In the shear deformation case, as shown in Fig. 4.11a, all architectures show a positive lateral pressure wave speed throughout the shear deformation except for the arrowhead unit cell in the 90° case. In the middle graph, Fig. 4.11b, again, all architectures but the arrowhead ones show an ability to maintain their pressure wave speeds. The lower graph in Fig. 4.11c depicts the development of the longitudinal pressure wave speeds over the shear deformation. The negative range of wave speeds for the arrowhead lattices is due to the subsequent flipping of the two central beams as explained in Section 4.1 and shown in Fig. 4.7. In Fig. 4.11 as before, the peaks and apparent infinite wave speeds stem from instabilities in the finite difference computation of the tangent stiffness tensor $\mathbb{C}^4$.

4.3. Impact performance of architectures

The impact protection of the different architectures is assessed by assembling the unit cells into a bigger patch. A schematic of the setup is shown in Fig. 4.12 and will be subsequently explained. Initially, these patches are globally compressed statically and dynamically at strain rates $\dot{H}$ of $2.5\,\mathrm{m\,s^{-1}}$, $5\,\mathrm{m\,s^{-1}}$, $7.5\,\mathrm{m\,s^{-1}}$, and $10\,\mathrm{m\,s^{-1}}$. Later, additional material is added to the sides to investigate the effects of lateral material involvement. The width of the impact loading is kept constant with the overall material width changing, resulting in width-to-impact ratios of $r_i = 1$, 1.5, 2, 3, and 5. The compression is induced with
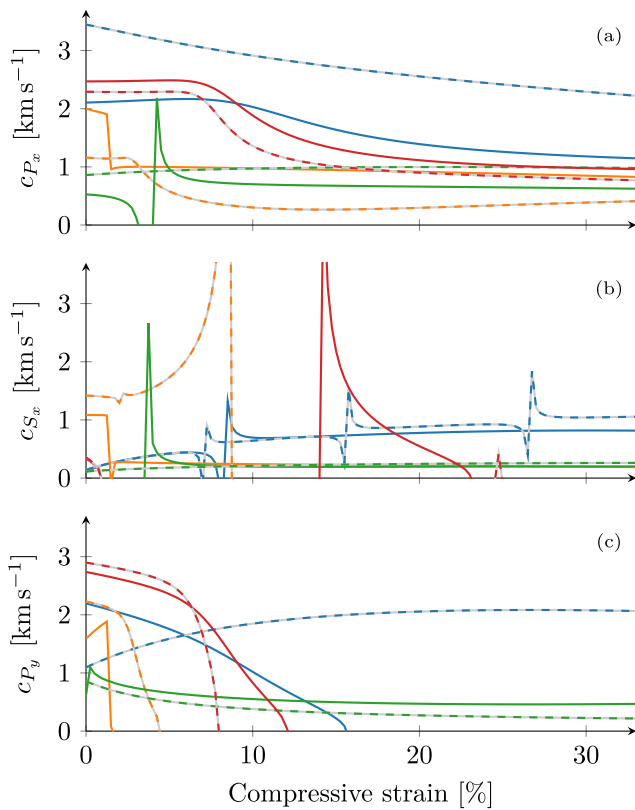
Fig. 4.10. Change of the lateral pressure and shear wave speed under planar compression, (a) shows the lateral pressure wave speed c_{P_x}, (b) shows the lateral shear wave speed c_{S_x}, (c) shows the pressure wave speed in impact direction c_{P_y}.

Fig. 4.11. Change of the lateral pressure and shear wave speed under shear, (a) shows the lateral pressure wave speed c_{P_x}, (b) shows the lateral shear wave speed c_{S_x}, (c) shows the pressure wave speed in impact direction c_{P_y}.

changing Dirichlet boundary conditions on the top boundary over the constant impact width, whilst the reaction forces are recorded. The bottom boundary is fully fixed and the sides are free.

During the computation, the displacements of the boundary subjected to movement $u_t(t)$ are stored as prescribed. The total force needed to achieve this displacement $f_t(t)$ and the total reaction force at the lower boundary $f_b(t)$ are recorded as well. In post-processing, the SEA for the undeformed volume under the impacted boundary (with initial height $h_0 \approx 1\,\mathrm{cm}$, width $w_0 \approx 1\,\mathrm{cm}$, and depth $d_0 = 10\,\mathrm{cm}$) is computed as[3]:

$$\mathrm{SEA}(t) = \frac{1}{\rho_0} \int_{\tau < t} \frac{u_t(\tau)}{h_0} \frac{f_t(\tau)}{w_0 d_0}. \tag{4.5}$$

The results of non-localized ($r_i = 1$), static ($\dot{H} = 0\,\mathrm{ms}^{-1}$) compression are shown in Fig. 4.13. It should be noted, that here only deformations up to 20 % are discussed in order to exclude interpenetration of beams, which may happen because contact is not considered in the numerical framework. In the graph the SEA is plotted against the compressive strain. The patches consisting of arrowhead unit cells (both rotated and not) could not be computed for the desired compression of 20 % due to a plethora of local buckling points in the singular structural members. The compression of the regular honeycomb structures (rotated and not rotated) requires most work especially in the later stages. Given the static nature of this experiment, only the static properties described in Section 4.1 have an effect. Here, especially the vertical stiffness during shear deformation as seen in Fig. 4.7a and the constrained stiffness related to the constrained stress–strain curve

in Fig. 4.4 are of importance. In both of these figures the regular honeycomb structures show the stiffest response over a wide range of deformation.

The next experiments are conducted with increased width of the patches ($r_i > 1$), but still under static loading ($\dot{H} = 0\,\mathrm{ms}^{-1}$) and reported in Fig. 4.14. The SEA is again plotted against the (local) compression, in Fig. 4.14a for $r_i = 3$ and in Fig. 4.14b for $r_i = 5$. Given the static context of this analysis, no fundamental changes are observed apart from the overall rise in work needed to compress the supported structure (compare the ranges of the y-axes of Figs. 4.13 and 4.14). It should be noted, that the patches of the arrowhead architectures could not be computed to the desired compression level again due to reasons as mentioned before.

Next, the dynamic behavior is investigated using moderately localized impact conditions ($r_i = 3$) and a set of strain rates ($\dot{H} = 5\,\mathrm{ms}^{-1}$ and $10\,\mathrm{ms}^{-1}$). The SEA of the different structures is shown in Fig. 4.15. The corresponding static compression is shown in Fig. 4.14a, whereas the upper graph (Fig. 4.15a) shows the SEA at a compression speed of $\dot{H} = 5\,\mathrm{ms}^{-1}$, which is doubled to $\dot{H} = 10\,\mathrm{ms}^{-1}$ in the lower graph Fig. 4.15b. At moderate impact speeds ($\dot{H} = 5\,\mathrm{ms}^{-1}$ in the upper graph), the difference between the structures in static compression are small, but the fact that the two regular honeycomb structure show a higher absorption compared to the auxetic structures, does not change. Only at the highest compression speeds ($10\,\mathrm{ms}^{-1}$), the re-entrant honeycomb, in its 90° configuration, is able to match with the regular honeycomb structures. As shown in Figs. 4.10a and 4.11a the re-entrant honeycomb shows the highest lateral pressure wave speeds, which in turn relates to a good involvement of the surrounding material. The regular honeycomb architectures show the highest values in the SEA throughout deformation, which is due to their ability to maintain a high stiffness in loading direction (as seen in Figs. 4.5a and 4.7a).

---

[3] Normalization for the initial volume is taking place to eliminate differences between the aspect ratios of the architectures and subsequent differences in initial volume.
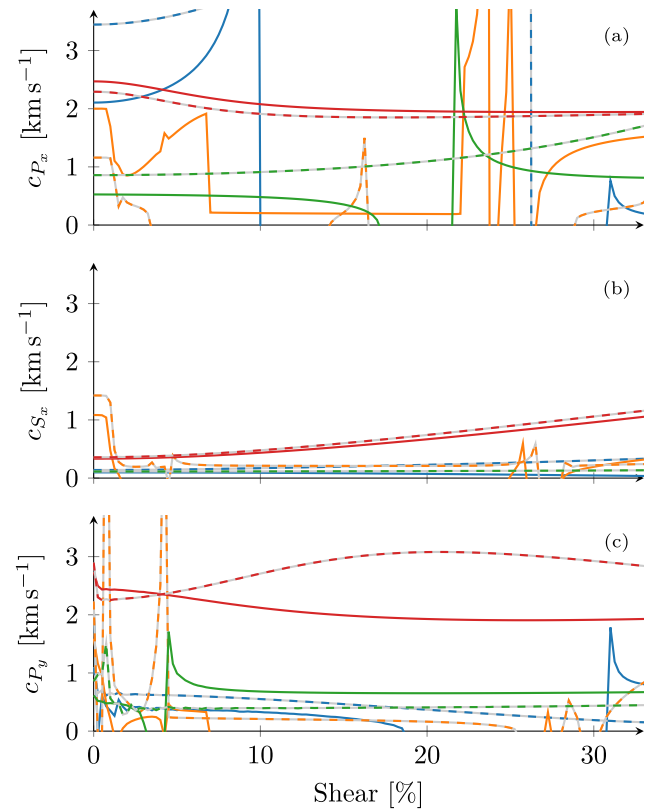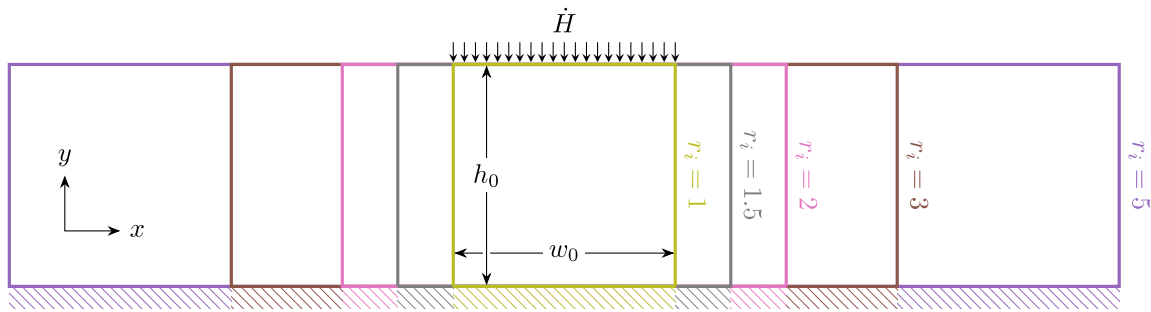
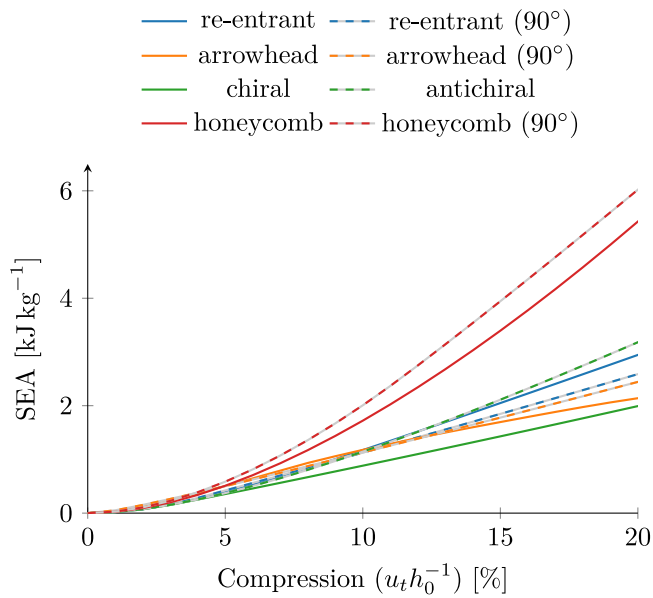**Fig. 4.12.** Sketch of the setup used for the simulations.

Fig. 4.13. SEA at non-localized ($r_i = 1$), static ($\dot{H} = 0\,\mathrm{ms}^{-1}$) compression.

Fig. 4.14. SEA at localized ((a) $r_i = 3$, (b) $r_i = 5$), static ($\dot{H} = 0\,\mathrm{ms}^{-1}$) compression.

Fig. 4.15. SEA at localized ($r_i = 3$), dynamic ((a) $\dot{H} = 5\,\mathrm{ms}^{-1}$, (b) $\dot{H} = 10\,\mathrm{ms}^{-1}$) compression.

A second set of investigations discussed in the following is conducted with stronger localized impact conditions ($r_i = 5$) at the same set of speeds ($\dot{H} = 5\,\mathrm{ms}^{-1}$ and $10\,\mathrm{ms}^{-1}$). In both graphs in Fig. 4.16, when compared to the corresponding graphs in Fig. 4.15, it can be observed that the effect of more lateral material is negligible for all architectures except from the rotated re-entrant honeycomb depicted in dashed blue. This effect, when comparing Figs. 4.15b and 4.16b even results in a better energy absorption capability of the re-entrant honeycomb structure compared to the regular honeycomb structure at high strain rates. This is due to the capability to involve the lateral material under strong deformation, which becomes more relevant with more lateral material (higher r_i) and at higher strain rates, as in Fig. 4.16a the rotated re-entrant honeycomb is not able to surpass the rotated regular honeycomb architecture. Fig. 4.17 further illustrates this effect. The top Fig. 4.17(a) depicts the left half of the regular honeycomb lattice and the right half of the re-entrant honeycomb lattice, both in their 90° orientation, in the undeformed state. The line thicknesses correspond to the beam thicknesses in the simulations, it should however be noted, that the re-entrant structure has been enlarged by about 9% in order to reach the same height and better visual comparability with the regular honeycomb. In the lower graphs, the deformed halves of the lattices are shown at ∼ 10% (Fig. 4.17(b)) and ∼ 20% (Fig. 4.17(c))

Fig. 4.16. SEA at localized ($r_i = 5$), dynamic ((a) $\dot{H} = 5\,\mathrm{ms}^{-1}$, (b) $\dot{H} = 10\,\mathrm{ms}^{-1}$) compression.
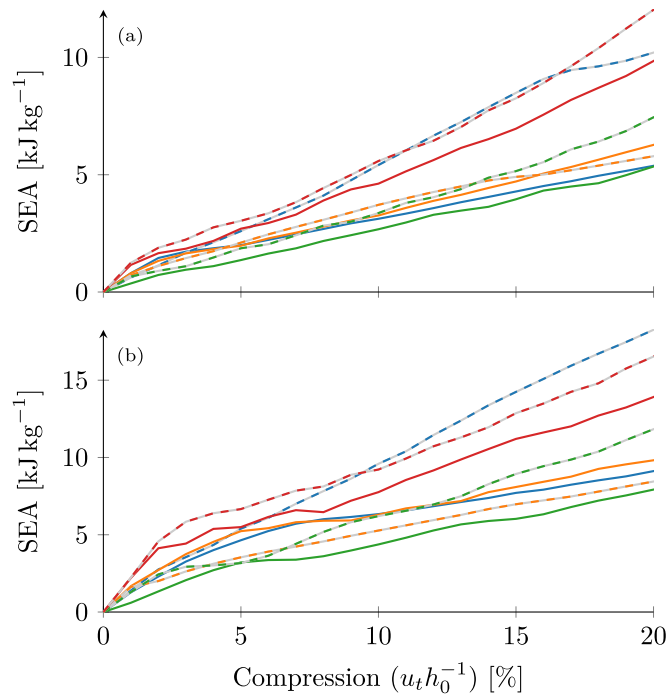
compression, with their respective undeformed configuration in the background. Here, the involvement of the surrounding material by lateral pressure wave speeds can be clearly seen. At 10 % compression, the re-entrant honeycomb lattice shows already deformation in the upper right corner of the lattice, whereas the regular honeycomb lattice shows deformation only up to roughly one third of the width. Up until this point, as can be seen in Fig. 4.16b, the regular honeycomb absorbs more energy, which can be motivated by the higher stiffness observed in Section 4.1. Only at later stages the higher material involvement as discussed in Section 4.2 contributes to the energy absorption. This can be more clearly seen in Fig. 4.17(c). Here the further involvement of the surrounding material for the regular honeycomb lattice is low when compared to the involvement of lateral material by the re-entrant honeycomb lattice on the right side, where the right edge shows deformation all the way down to the back face. These deformations clearly show the activation of the lateral material, leading to the dispersion of the impact energy into kinetic and elastic potential energy of the material far away from the impact zone. However, for the example of the rotated regular honeycomb structure, it can be seen that this effect does not simply originate from a negative Poisson's ratio, but rather from the ability to maintain its stiffness at different deformations modes as discussed in Section 4.1 whilst at the same time providing the ability to involve the lateral material as discussed in Section 4.2.

In Fig. 4.18 the effect of the lateral material as expressed by the impact ratio r_i is shown as the SEA is plotted against the impact ratio for different levels of compression. In this graph, it is shown that while most structures tend to obtain less additional benefit from additional lateral material, the rotated re-entrant honeycomb exhibits even at $r_i = 5$ a positive slope of the SEA-curve, resulting in an added benefit of a further extension of the lattice to the sides, in other words for higher r_i values. This suggests, that when analyzing the elastic energy absorption capabilities of different architected materials, the Poisson's ratio in itself is not sufficient in order to determine the performance of a particular architecture in impact scenarios.

5. Varying the effective properties

As mentioned before, all observations have been made using the target properties $E_y^\star = 300\,\mathrm{MPa}$ and $\rho_{\mathrm{rel}}^\star = 0.1$. In the following

section, these observations are summarized and their applicability and limitations in a wider range of properties are shown. For this, both $E_y^\star$ and $\rho_{\mathrm{rel}}^\star$ are individually increased and decreased by a third. This results in three measures $E_y^\star = 200\,\mathrm{MPa}$, $300\,\mathrm{MPa}$, and $400\,\mathrm{MPa}$ for the effective Young's modulus and $\rho_{\mathrm{rel}}^\star = 0.067$, 0.100, and 0.133 for the relative density and all nine combinations of the two effective measures are investigated. The structures are first designed following the optimization procedure described in Section 2.2 and subsequently investigated in the same way as described earlier. The behavior at different configurations is shown in Fig. 5.1, while the structures itself together with their properties can be found in Appendix A. In the figure, the SEA is plotted for different impact ratios r_i at 20 % compression level for dynamic compression at $\dot{H} = 10\,\mathrm{ms}^{-1}$. The central graph shows the observations at $E_y^\star = 300\,\mathrm{MPa}$ and $\rho_{\mathrm{rel}}^\star = 0.1$.

As discussed earlier, the honeycomb structures show the highest absorption of energy for no or small lateral material around the impact zone, due to their high stiffness during pure shear and resistance during planar compression. In Section 4.1 the development of the Young's modulus E_y for uniaxial compression, planar compression and pure shear deformation is shown. It is demonstrated, that structures where the load is carried predominately by axial forces rather than bending moments experience an increase in E_y whereas structures with more bending loading during deformation experience a decrease.

The only structure able to gain further benefits from more lateral material is the re-entrant honeycomb in its 90° configuration, due to the consistently high lateral pressure wave speeds allowing the involvement of a wide amount of lateral material. This is due to the fact, that next to the pure static resistance to impact, also the dynamic properties play an important role in the response of a patch towards localized, high rate compression. These dynamic properties are reported in Section 4.2. Here it is also shown, that the lateral shear wave speeds are smaller than the lateral pressure wave speeds for all architectures. Section 4.3 relates a consistently high lateral pressure wave speed to the energy absorption of the architectures in impact events. Planar compression and pure shear deformation are considered the most relevant deformation patterns in impact scenarios. For these two deformation patterns, it is essential for both critical factors, stiffness in the loading direction (E_y), and the lateral pressure wave speed (c_{P_x}), to remain at a high level in order to absorb the most impact energy. Comparable results can be achieved in all investigated configurations.

It should be noted, that the rotated re-entrant honeycomb structure at $E_y^\star = 200\,\mathrm{MPa}$ and $\rho_{\mathrm{rel}}^\star = 0.1$, the antichiral structures at $\rho_{\mathrm{rel}}^\star = 0.067$, and the rotated regular honeycomb structures at $\rho_{\mathrm{rel}}^\star = 0.133$ show a different behavior than their counterparts at $E_y^\star = 300\,\mathrm{MPa}$ and $\rho_{\mathrm{rel}}^\star = 0.1$. However, these different observations can be explained by differences in the evolution of the equivalent properties during the discussed simple deformation modes.

6. Conclusion

The Poisson's ratio alone is not sufficient to explain the differences in elastic impact mitigation behavior between different lattice architectures. The working mechanisms of the lattice must be taken into account as well to explain these differences. While the exact internal deformation patterns are complex and highly dependent on the exact boundary conditions, a clear dependency can be established between the static properties and the ability of the architectures to adsorb and disperse energy. The evolution of the stiffness in the direction of impact, as well as the lateral pressure wave speed through the deformation modes typical for impact scenarios, namely planar compression and pure shear deformation, give an indication of the performance of the architecture in highly localized impact scenarios. First, the stiffness in loading direction must remain sufficiently high under both planar compression and pure shear deformation. In particular, architectures that exhibit folding in the impact direction, which results in higher
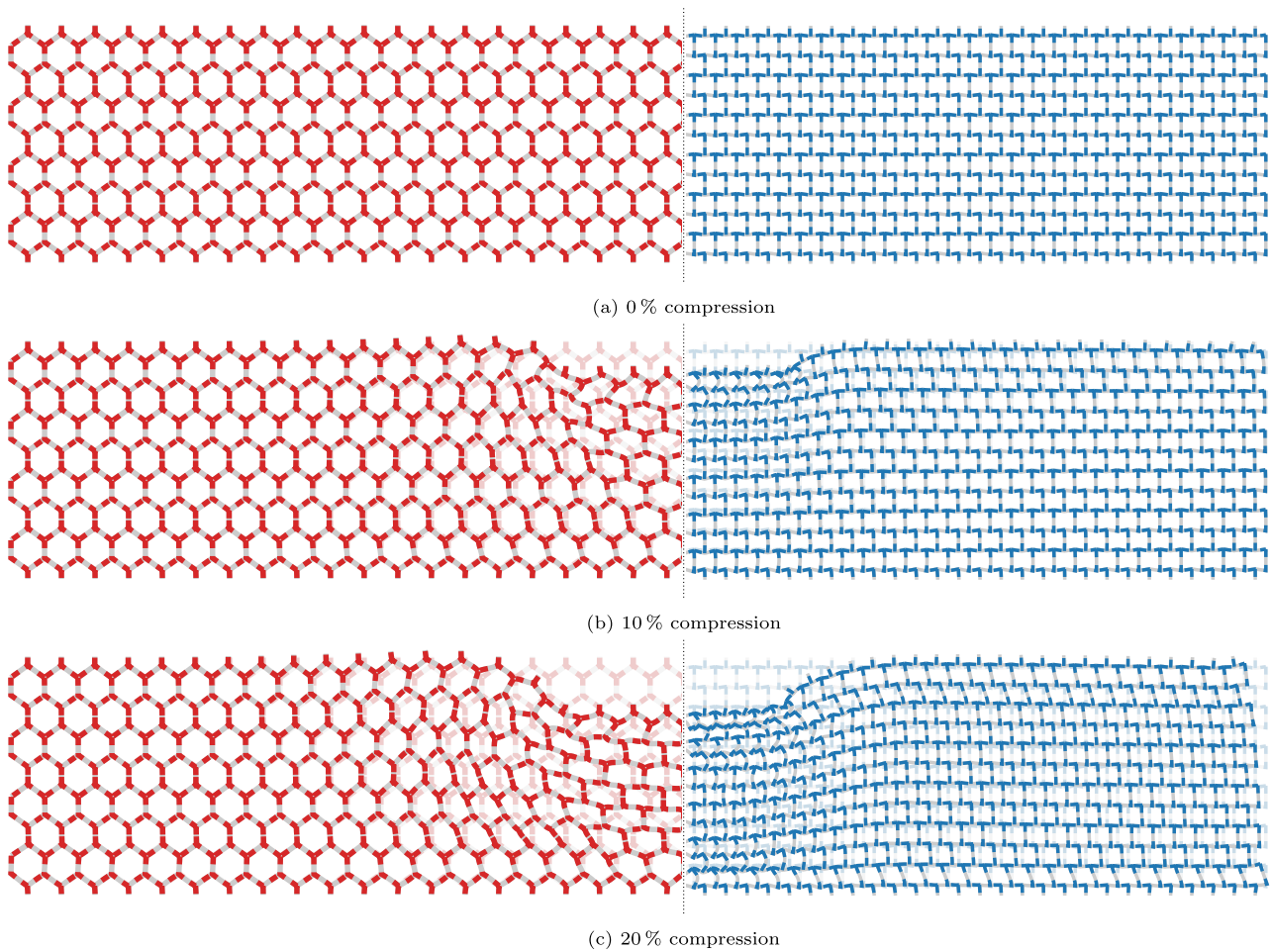
(a) 0 % compression

(b) 10 % compression

(c) 20 % compression

Fig. 4.17. Comparison of the regular and re-entrant honeycomb under localized ($r_i = 5$), dynamic ($\dot{H} = 10\,\mathrm{ms}^{-1}$) compression.
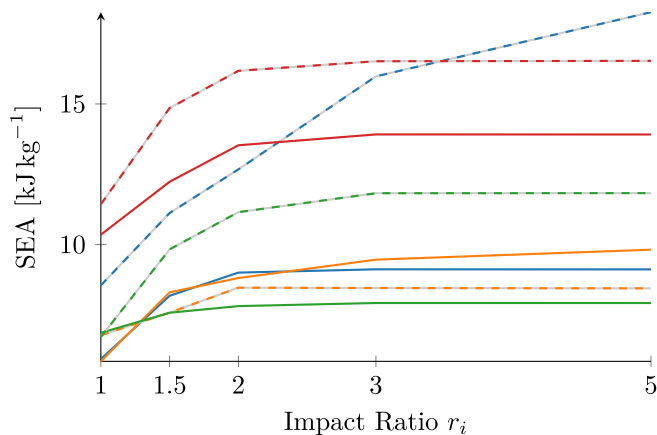
Fig. 4.18. SEA against impact ratio at $\dot{H} = 10\,\mathrm{ms}^{-1}$ and a strain level of 20 %.

a solid foundation for further investigation into dynamic deformation patterns of architected materials by demonstrating the effects of geometry in an elastic setting.

CRediT authorship contribution statement

T. Gärtner: Writing – original draft, Visualization, Validation, Software, Methodology, Investigation, Data curation, Conceptualization. **S.J. van den Boom:** Writing – review & editing, Supervision, Methodology, Conceptualization. **J. Weerheijm:** Writing – review & editing, Funding acquisition, Conceptualization. **L.J. Sluys:** Writing – review & editing, Supervision, Project administration, Methodology, Funding acquisition, Conceptualization.

Declaration of competing interest

The authors declare that they have no known competing financial interests or personal relationships that could have appeared to influence the work reported in this paper.

Data availability

Data will be made available upon request.

Acknowledgments

axial loading of the members, show stiffer responses throughout deformation. However, they are prone to buckling in their axially loaded members, which can cancel this effect. Second, the lateral material involvement, here estimated by the lateral pressure wave speed, must remain at a sufficiently high level during deformation to allow the impact energy to be distributed to the surrounding material.

The choice of the optimal material architecture is a difficult task when designing protection concepts for different kinds of threats and environments. This work provides the design engineer with a first insight into the effects of different architectural choices in mechanical metamaterials used in impact protection scenarios. It also provides

Fig. 5.1. SEA at 20 % compression at $\dot{H} = 10\,\text{ms}^{-1}$.

Table A.1

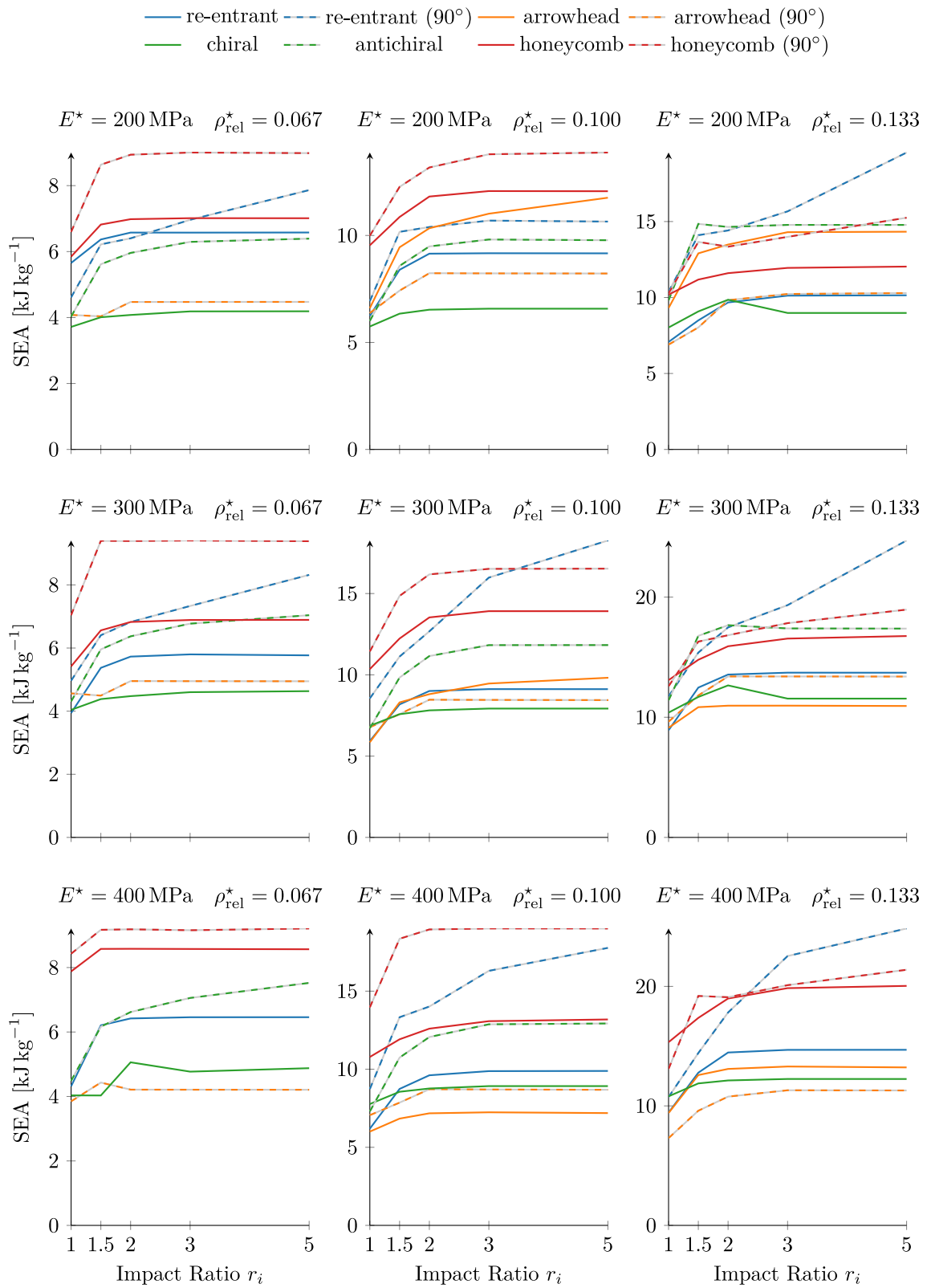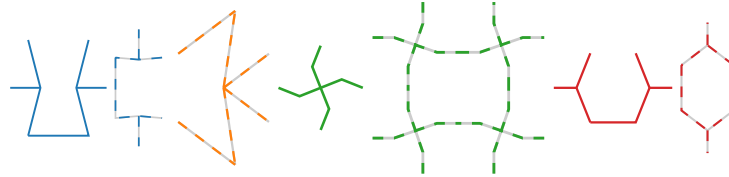Resulting properties and unit cells of the investigated architectures with target properties $E_y^\star = 200\,\text{MPa}, \rho_{\text{rel}}^\star = 0.067$.

Geometry	t	α [°]	β [°]	r	ρ_{rel}	E_y [MPa]	E_x [MPa]	ν_{yx}	ν_{xy}	G_{xy} [MPa]	G_{yx} [MPa]
re-entrant	0.032	75.59	–	0.82	0.067	198	14	−3.77	−0.26	2	2
re-entrant (90°)	0.028	84.99	–	0.39	0.067	195	2,465	−0.21	−2.69	5	5
arrowhead (90°)	0.025	8.55	53.06	–	0.067	194	8	−4.79	−0.20	1,291	1,291
chiral	0.058	21.71	–	–	0.067	199	199	−0.38	−0.38	67	4
antichiral	0.061	19.01	–	–	0.067	198	198	−0.70	−0.70	3	3
honeycomb	0.050	111.82	–	0.82	0.067	199	95	1.42	0.68	16	16
honeycomb (90°)	0.045	127.38	–	0.72	0.067	199	55	1.87	0.52	18	18

Table A.2

Resulting properties and unit cells of the investigated architectures with target properties $E_y^\star = 200\,\text{MPa}, \rho_{\text{rel}}^\star = 0.100$.

Geometry	t	α [°]	β [°]	r	ρ_{rel}	E_y [MPa]	E_x [MPa]	ν_{yx}	ν_{xy}	G_{xy} [MPa]	G_{yx} [MPa]
re-entrant	0.037	65.33	–	0.62	0.100	198	74	−1.60	−0.60	6	6
re-entrant (90°)	0.034	63.18	–	0.46	0.100	196	208	−0.94	−1.00	6	6
arrowhead	0.025	5.27	70.70	–	0.100	198	1,873	−0.25	−2.39	1,398	1,397
arrowhead (90°)	0.031	15.91	62.35	–	0.100	199	60	−1.77	−0.53	1,555	1,559
chiral	0.073	31.56	–	–	0.100	200	200	−0.38	−0.38	97	68
antichiral	0.080	30.17	–	–	0.100	199	200	−0.70	−0.70	9	9
honeycomb	0.094	124.94	–	1.13	0.100	199	306	0.79	1.21	96	96
honeycomb (90°)	0.095	116.11	–	1.16	0.100	200	392	0.69	1.36	81	81
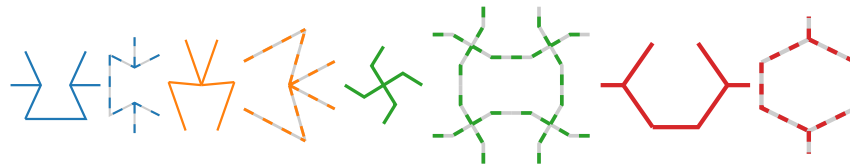
Appendix A. Structural configurations

A more detailed description of the tuning process for each architecture is described here. As can be seen in Fig. 2.3(a), the re-entrant honeycomb has three variables that define the geometry, namely the sizes of the base b and the tilted bars l as well as the angle of these tilted bars α. Finally, the thickness of the bars d is a parameter to be determined. This study assumes (linear) elastic material behavior. Structures with geometric similitude can be assumed to have no difference in their behavior. Therefore, the values of b, l, and d by themselves are not important, but the ratio between them is. We chose the ratio of the tilted bar length to the base length $r = \frac{l}{b}$ and the ratio of the thickness to the base length $t = \frac{d}{b}$. In this study, the angle α ranges from 20° to 85°, the beam length ratio t ranges from $\frac{1}{3}$ to $\frac{4}{3}$, and the beam thickness ratio t ranges from 0.01 to 0.1. For small angles, the re-entrant beams may not intersect, so the additional constraint $r < \frac{1}{2\cos\alpha}$ is introduced.

The arrowhead structure is defined by the two angles $\alpha \in (5°, 60°)$, $\beta \in (45°, 75°)$ (see Fig. 2.4(a)) and the thickness of the beams relative to the height of the structure $t = \frac{d}{h} \in (0.01, 0.1)$, as can be seen in Fig. 2.4(a). To get realistic structures, the constraint $3\tan\alpha < \tan\beta$ was added.

For the second auxetic mechanism, as explained in Section 2.1, a chiral and an anti-chiral lattice have been selected. As can be seen in Figs. 2.1(a) and 2.2(a), the only parameters to set are the angle $\alpha \in (5°, 60°)$ and the thickness of the beams relative to the width of the unit cell $t = \frac{d}{b} \in (0.01, 0.1)$. Since the antichiral unit cell is based on the chiral one, the parameters and their respective ranges are identical.

Finally, the properties of a non-auxetic architecture are also examined for comparison. For simplicity, the same parameter range is

chosen as for the re-entrant honeycomb, but with angles $\alpha \in (95°, 145°)$, resulting in a positive Poisson's ratio (see Gibson et al., 1997).

For each considered architecture, in a first step, the elastic properties in the undeformed configuration are recorded for all valid combinations in a full factorial exploration space. These results are then used to create a (linearized) mapping for the four linear elastic constants of an orthotropic material in 2D as well as the relative density $\mathcal{P} \mapsto \left(E_y, E_x, \nu_{yx}, G, \rho_{\text{rel}}\right)$. Where $\mathcal{P}$ is the point in the design space that describes the variables described above. Using this mapping, a target function is defined by calculating the root sum squared of the error terms. In the case of the desired vertical Young's modulus $E_y^\star = 300\,\text{MPa}$ and relative density $\rho_{\text{rel}}^\star = 0.1$, this results in the following objective function

$$t(\mathcal{P}) = \sqrt{\left(\frac{E_y(\mathcal{P}) - E_y^\star}{E_y^\star}\right)^2 + \left(\frac{\rho_{\text{rel}}(\mathcal{P}) - \rho_{\text{rel}}^\star}{\rho_{\text{rel}}^\star}\right)^2} \tag{A.1}$$

This objective function is now minimized in the parameter spaces shown in Table 2.1 with the reported constraints using the *scipy*[4] implementation of the DIRECT optimizer.

With the procedure described above, all architectures are tuned to exhibit the desired properties. All combinations of $E_y^\star = 200\,\text{MPa}$, 300 MPa, and 400 MPa and $\rho_{\text{rel}}^\star = 0.067$, 0.100, and 0.133 are designed. The resulting orthotropic material properties are given in Tables A.1 to A.9 accepting some discrepancy between the linearized target function space and the actual computations. The corresponding configurations are shown below the tables.

---

[4] version 1.9.2.

Table A.3

Resulting properties and unit cells of the investigated architectures with target properties $E_y^\star = 200$ MPa, $\rho_{\rm rel}^\star = 0.133$.

Geometry	t	α [°]	β [°]	r	$\rho_{\rm rel}$	E_y [MPa]	E_x [MPa]	ν_{yx}	ν_{xy}	G_{xy} [MPa]	G_{yx} [MPa]
re-entrant	0.035	53.37	–	0.35	0.133	199	801	−0.47	−1.89	11	11
re-entrant (90°)	0.075	84.29	–	0.80	0.133	199	8,025	−0.11	−4.55	36	36
arrowhead	0.035	26.84	68.20	–	0.133	198	125	−1.22	−0.77	1,401	1,401
arrowhead (90°)	0.028	23.86	73.89	–	0.133	199	462	−0.63	−1.46	1,136	1,136
chiral	0.082	38.53	–	–	0.133	200	200	−0.38	−0.38	19	178
antichiral	0.091	38.87	–	–	0.133	200	200	−0.69	−0.69	17	17
honeycomb	0.052	135.63	–	0.39	0.133	198	3,877	0.20	3.94	57	57
honeycomb (90°)	0.099	96.35	–	1.03	0.133	199	7,997	0.12	4.72	73	73

Table A.4

Resulting properties and unit cells of the investigated architectures with target properties $E_y^\star = 300$ MPa, $\rho_{\rm rel}^\star = 0.067$.

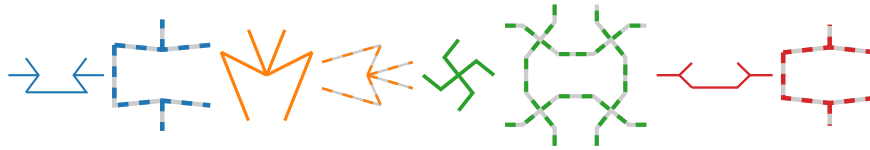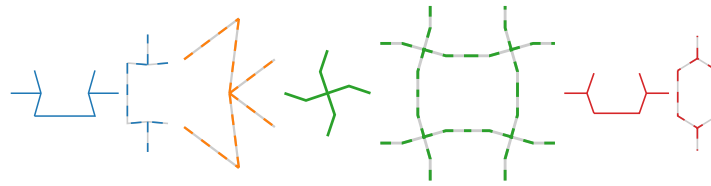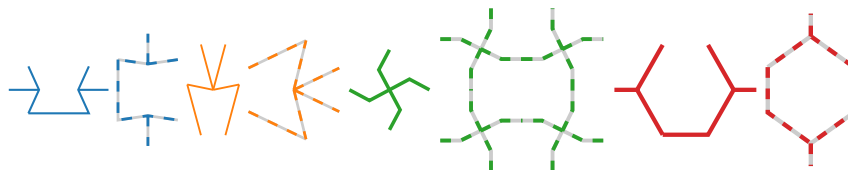| Geometry	t	α [°]	β [°]	r	$\rho_{\rm rel}$	E_y [MPa]	E_x [MPa]	ν_{yx}	ν_{xy}	G_{xy} [MPa]	G_{yx} [MPa]
re-entrant	0.025	74.07	–	0.39	0.067	296	138	−1.40	−0.66	3	3
re-entrant (90°)	0.027	85.00	–	0.34	0.069	292	2,611	−0.24	−2.17	5	5
arrowhead (90°)	0.025	7.15	53.27	–	0.067	290	9	−5.59	−0.17	1,353	1,353
chiral	0.060	18.55	–	–	0.067	299	299	−0.38	−0.38	10	−16
antichiral	0.063	15.84	–	–	0.067	298	298	−0.69	−0.69	4	4
honeycomb	0.035	109.26	–	0.47	0.067	298	252	1.04	0.88	10	10
honeycomb (90°)	0.036	121.56	–	0.51	0.067	298	94	1.74	0.55	12	12

Table A.5

Resulting properties and unit cells of the investigated architectures with target properties $E_y^\star = 300$ MPa, $\rho_{\rm rel}^\star = 0.100$.

Geometry	t	α [°]	β [°]	r	$\rho_{\rm rel}$	E_y [MPa]	E_x [MPa]	ν_{yx}	ν_{xy}	G_{xy} [MPa]	G_{yx} [MPa]
re-entrant	0.035	65.62	–	0.43	0.100	297	273	−1.00	−0.92	8	8
re-entrant (90°)	0.046	81.67	–	0.50	0.100	297	2,937	−0.26	−2.60	15	15
arrowhead	0.021	11.60	74.90	–	0.100	296	468	−0.73	−1.16	924	924
arrowhead (90°)	0.030	13.81	64.34	–	0.100	295	80	−1.85	−0.50	1,583	1,583
chiral	0.078	28.11	–	–	0.100	299	299	−0.38	−0.38	53	19
antichiral	0.085	26.09	–	–	0.100	299	299	−0.69	−0.69	10	10
honeycomb	0.094	119.69	–	1.14	0.100	299	243	1.08	0.88	87	87
honeycomb (90°)	0.096	125.63	–	1.17	0.100	299	187	1.24	0.77	100	100

Appendix B. Boundary conditions and tangent properties

In this Appendix, a more detailed description of the implementation of the PBCs and the subsequent computation of the elastic tangent properties using these, as discussed in Section 3.1, is given.

B.1. Periodic boundary conditions

As can be seen in Fig. B.1, the boundary of a (rectangular) unit cell is split into 4 sections $\Gamma_T, \Gamma_R, \Gamma_B, \Gamma_L$ such that Γ_T represents all the nodes on the top side of the unit cell, Γ_R all the nodes on the right side, Γ_B all on the bottom side, and finally Γ_L the nodes on the left side. This figure shows for all 5 investigated unit cells (re-entrant honeycomb unit cell in Fig. B.1(a), arrowhead unit cell in Fig. B.1(b), chiral unit

cell in Fig. B.1(c), antichiral unit cell in Fig. B.1(d), and the regular honeycomb unit cell in Fig. B.1(e)) the empty corners. We therefore add 'ghost' nodes, not connected to the rest of the mesh, in the corners for the application of boundary conditions as described in the following. The four nodes in the corners start with node 0 at the bottom left side and are then numbered counter-clockwise.

The sets for corresponding sides need to be ordered in a way, such that they correspond towards each other, i.e. in a rectangular unit cell for every node on the bottom edge, we need to find a node on the top edge, for which the relationship

$$X_T = X_B + \begin{bmatrix} 0 \\ h \end{bmatrix} \tag{B.1}$$

of the respective reference position vectors X holds, where h is the height of the unit cell. With its width w, a similar relationship holds

Table A.6

Resulting properties and unit cells of the investigated architectures with target properties $E_y^\star = 300\,\text{MPa}, \rho_{\text{rel}}^\star = 0.133$.

Geometry	t	$\alpha\,[°]$	$\beta\,[°]$	r	ρ_{rel}	$E_y\,[\text{MPa}]$	$E_x\,[\text{MPa}]$	ν_{yx}	ν_{xy}	$G_{xy}\,[\text{MPa}]$	$G_{yx}\,[\text{MPa}]$
re-entrant	0.045	61.08	–	0.57	0.133	298	191	−1.21	−0.78	11	11
re-entrant (90°)	0.070	83.33	–	0.69	0.133	298	6,987	−0.15	−3.55	37	37
arrowhead	0.025	42.99	75.37	–	0.133	294	24	−3.43	−0.28	686	686
arrowhead (90°)	0.041	18.86	62.75	–	0.133	299	133	−1.44	−0.64	1,911	1,911
chiral	0.089	35.19	–	–	0.133	300	300	−0.38	−0.38	156	35
antichiral	0.099	34.70	–	–	0.133	299	299	−0.69	−0.69	19	19
honeycomb	0.097	131.09	–	0.83	0.133	299	1,319	0.45	1.99	162	162
honeycomb (90°)	0.099	99.51	–	0.94	0.133	299	5,108	0.20	3.43	85	85

Table A.7

Resulting properties and unit cells of the investigated architectures with target properties $E_y^\star = 400\,\text{MPa}, \rho_{\text{rel}}^\star = 0.067$.

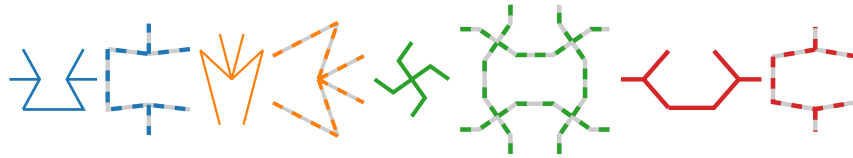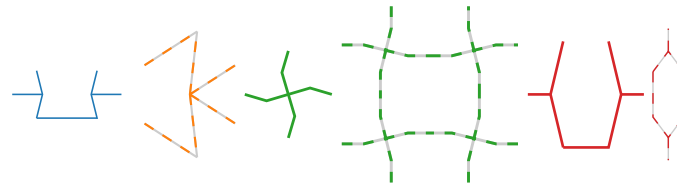| Geometry	t	$\alpha\,[°]$	$\beta\,[°]$	r	ρ_{rel}	$E_y\,[\text{MPa}]$	$E_x\,[\text{MPa}]$	ν_{yx}	ν_{xy}	$G_{xy}\,[\text{MPa}]$	$G_{yx}\,[\text{MPa}]$
re-entrant	0.026	76.05	–	0.40	0.067	398	136	−1.63	−0.56	4	4
arrowhead (90°)	0.023	6.54	57.28	–	0.067	392	14	−5.12	−0.18	1,386	1,386
chiral	0.061	16.44	–	–	0.067	399	399	−0.37	−0.37	2	−1
antichiral	0.064	13.85	–	–	0.067	395	395	−0.68	−0.68	4	4
honeycomb	0.059	103.41	–	1.20	0.067	397	28	3.67	0.26	14	14
honeycomb (90°)	0.031	143.10	–	0.56	0.067	395	13	5.50	0.17	10	10

Table A.8

Resulting properties and unit cells of the investigated architectures with target properties $E_y^\star = 400\,\text{MPa}, \rho_{\text{rel}}^\star = 0.100$.

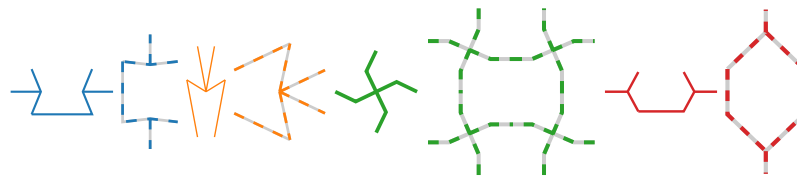| Geometry	t	$\alpha\,[°]$	$\beta\,[°]$	r	ρ_{rel}	$E_y\,[\text{MPa}]$	$E_x\,[\text{MPa}]$	ν_{yx}	ν_{xy}	$G_{xy}\,[\text{MPa}]$	$G_{yx}\,[\text{MPa}]$
re-entrant	0.035	67.69	–	0.40	0.100	397	343	−1.02	−0.88	8	8
re-entrant (90°)	0.045	83.36	–	0.46	0.100	394	4,132	−0.23	−2.41	16	16
arrowhead	0.015	31.67	79.43	–	0.099	380	36	−3.18	−0.30	435	435
arrowhead (90°)	0.030	12.18	64.54	–	0.100	395	85	−2.05	−0.44	1,633	1,633
chiral	0.081	25.65	–	–	0.100	399	399	−0.37	−0.37	33	44
antichiral	0.088	23.33	–	–	0.100	398	398	−0.69	−0.69	11	11
honeycomb	0.054	118.49	–	0.49	0.100	397	927	0.61	1.44	37	37
honeycomb (90°)	0.092	133.79	–	1.17	0.100	399	96	1.99	0.48	106	106

Table A.9

Resulting properties and unit cells of the investigated architectures with target properties $E_y^\star = 400\,\text{MPa}, \rho_{\text{rel}}^\star = 0.133$.

| Geometry	t	$\alpha\,[°]$	$\beta\,[°]$	r	ρ_{rel}	$E_y\,[\text{MPa}]$	$E_x\,[\text{MPa}]$	ν_{yx}	ν_{xy}	$G_{xy}\,[\text{MPa}]$	$G_{yx}\,[\text{MPa}]$
re-entrant	0.045	62.12	–	0.49	0.133	397	340	−1.03	−0.89	13	13
re-entrant (90°)	0.056	73.13	–	0.54	0.133	398	1,497	−0.47	−1.78	23	23
arrowhead	0.026	33.15	74.81	–	0.133	397	71	−2.30	−0.41	896	896
arrowhead (90°)	0.025	18.09	76.47	–	0.133	395	747	−0.67	−1.27	978	978
chiral	0.094	32.74	–	–	0.133	399	399	−0.37	−0.37	28	−69
honeycomb	0.100	127.62	–	0.83	0.133	399	1,195	0.55	1.64	161	161
honeycomb (90°)	0.092	98.75	–	0.82	0.133	399	5,941	0.20	3.05	79	79
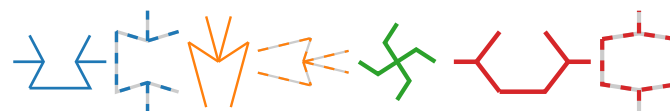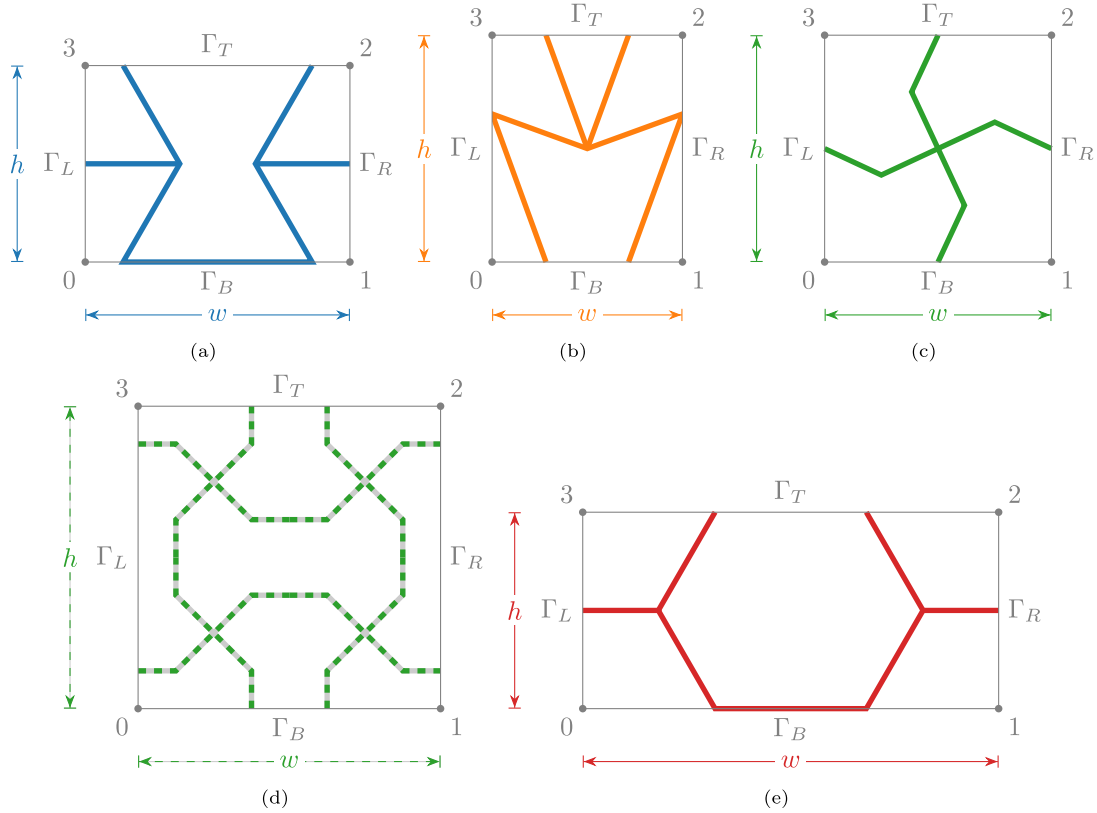
Fig. B.1. Unit cells of (a) the re-entrant honeycomb, (b) the arrowhead structure, (c) the chiral structure, (d) the antichiral structure, and (e) the honeycomb structure with notation used for establishing the PBCs.

to identify corresponding nodes between the left and right edges:

$$X_R = X_L + \begin{bmatrix} w \\ 0 \end{bmatrix}. \tag{B.2}$$

After having identified all nodes that need to be taken into account, it is made sure that the rotation of one node is equal to the rotation of the corresponding node on the opposite side by enforcing the following two boundary conditions on the rotational displacement vectors $\boldsymbol{\vartheta}$:

$$\boldsymbol{\vartheta}_{iT} = \boldsymbol{\vartheta}_{iB}, \quad \forall iT \in \Gamma_T, iB \in \Gamma_B \mid X_{iT} = X_{iB} + \begin{bmatrix} 0 \\ h \end{bmatrix}, \tag{B.3}$$

$$\boldsymbol{\vartheta}_{iR} = \boldsymbol{\vartheta}_{iL}, \quad \forall iR \in \Gamma_R, iL \in \Gamma_L \mid X_{iR} = X_{iL} + \begin{bmatrix} w \\ 0 \end{bmatrix}. \tag{B.4}$$

The translational displacement vectors $\boldsymbol{u}$ are now coupled via the controlling nodes at the corresponding sides as (sets are omitted for better readability)

$$u_{iT} = u_{iB} + (u_3 - u_0), \tag{B.5}$$

$$u_{iR} = u_{iL} + (u_1 - u_0), \tag{B.6}$$

while the corner nodes are fixed to enforce the desired displacement gradient $H_{ij} = \frac{\partial u_i}{\partial X_j}$,

$$u_0 = \begin{bmatrix} 0 \\ 0 \end{bmatrix} \quad u_1 = H \cdot \begin{bmatrix} w \\ 0 \end{bmatrix} \quad u_3 = H \cdot \begin{bmatrix} 0 \\ h \end{bmatrix}. \tag{B.7}$$

It should be noted, that the *ghost* nodes are not connected to any element in the FE implementation and thus do not contribute to the internal force vector or stiffness matrix, but their effect stems from constraining the system whilst using them as helper nodes. Also, in order to prevent rigid body movement, a single node connected to the structure needs to have all translational degrees of freedom (DOFs) being equal to 0.

The 1st Piola–Kirchhoff stress tensor $\boldsymbol{P}$ is subsequently calculated based on its definition

$$\frac{f}{\Gamma_0} = P n_0. \tag{B.8}$$

Where $\boldsymbol{f}$ are the forces on the surface, Γ_0 is the area of the undeformed surface and $\boldsymbol{n}_0$ is the normal to the undeformed surface. One can now rearrange it for the different surfaces and average over two opposite surfaces for numerical accuracy:

$$P_{11} = \frac{f_1(R) - f_1(L)}{\Gamma_R + \Gamma_L} \tag{B.9}$$

$$P_{12} = \frac{f_1(T) - f_1(B)}{\Gamma_T + \Gamma_B} \tag{B.10}$$

$$P_{21} = \frac{f_2(R) - f_2(L)}{\Gamma_R + \Gamma_L} \tag{B.11}$$

$$P_{22} = \frac{f_2(T) - f_2(B)}{\Gamma_T + \Gamma_B} \tag{B.12}$$

B.2. Computation of the tangent properties

We start from the relationships

$$\delta P = \mathbb{C}^4 : \delta H \tag{B.13}$$

and

$$\delta H = \mathbb{S}^4 : \delta P. \tag{B.14}$$

In order to simplify notation, $\boldsymbol{P}, \boldsymbol{H}$ are now column-vectors and $\mathbb{S}^4, \mathbb{C}^4$ are now the matrices $[\boldsymbol{S}], [\boldsymbol{C}]$

$$\delta \begin{bmatrix} P_{11} \\ P_{12} \\ P_{21} \\ P_{22} \end{bmatrix} = \begin{bmatrix} c_{1111} & c_{1112} & c_{1121} & c_{1122} \\ c_{1211} & c_{1212} & c_{1221} & c_{1222} \\ c_{2111} & c_{2112} & c_{2121} & c_{2122} \\ c_{2211} & c_{2212} & c_{2221} & c_{2222} \end{bmatrix} \delta \begin{bmatrix} H_{11} \\ H_{12} \\ H_{21} \\ H_{22} \end{bmatrix} \tag{B.15}$$

or with the index combination $(11) \Rightarrow 1, (12) \Rightarrow 2, (21) \Rightarrow 3, (22) \Rightarrow 4$

$$\delta \begin{bmatrix} P_1 \\ P_2 \\ P_3 \\ P_4 \end{bmatrix} = \begin{bmatrix} c_{11} & c_{12} & c_{13} & c_{14} \\ c_{21} & c_{22} & c_{23} & c_{24} \\ c_{31} & c_{32} & c_{33} & c_{34} \\ c_{41} & c_{42} & c_{43} & c_{44} \end{bmatrix} \delta \begin{bmatrix} H_1 \\ H_2 \\ H_3 \\ H_4 \end{bmatrix}. \tag{B.16}$$

The tangent stiffness matrix $[C]$ is computed as described in Section 3.1 and the tangent compliance matrix $[S]$ is afterwards computed by

$$[S] = (0.5[C] + 0.5[C]^T)^{-1}, \tag{B.17}$$

where the symmetrization of the stiffness is done to minimize numerical errors.

For the derivation of the (linearized) Young's modulus and Poisson's ratio, we need a relation between δP_i and δH_i, where the orthogonal stress is zero, whilst the orthogonal strain is free

$$\begin{bmatrix} \delta H_1 \\ 0 \\ 0 \\ \delta H_2 \end{bmatrix} = \begin{bmatrix} s_{11} & s_{12} & s_{13} & s_{14} \\ s_{21} & s_{22} & s_{23} & s_{24} \\ s_{31} & s_{32} & s_{33} & s_{34} \\ s_{41} & s_{42} & s_{43} & s_{44} \end{bmatrix} \begin{bmatrix} \delta P_1 \\ \delta P_2 \\ \delta P_3 \\ 0 \end{bmatrix}. \tag{B.18}$$

Starting with the third line of (B.18), we obtain

$$0 = s_{31}\delta P_1 + s_{32}\delta P_2 + s_{33}\delta P_3, \tag{B.19}$$

$$\delta P_3 = \frac{-s_{31}}{s_{33}}\delta P_1 + \frac{-s_{32}}{s_{33}}\delta P_2, \tag{B.20}$$

$$\delta P_3 = f_{31}\delta P_1 + f_{32}\delta P_2. \tag{B.21}$$

Inserting now (B.21) in the second line of (B.18), we obtain

$$0 = s_{21}\delta P_1 + s_{22}\delta P_2 + s_{23}\delta P_3, \tag{B.22}$$

$$0 = s_{21}\delta P_1 + s_{22}\delta P_2 + s_{23}(f_{31}\delta P_1 + f_{32}\delta P_2), \tag{B.23}$$

$$0 = (s_{21} + s_{23}f_{31})\delta P_1 + (s_{22} + s_{23}f_{32})\delta P_2, \tag{B.24}$$

$$\delta P_2 = \frac{-s_{21} - s_{23}f_{31}}{s_{22} + s_{23}f_{32}}\delta P_1, \tag{B.25}$$

$$\delta P_2 = f_{21}\delta P_1. \tag{B.26}$$

This can now be inserted into (B.21)

$$\delta P_3 = f_{31}\delta P_1 + f_{32}\delta P_2, \tag{B.27}$$

$$\delta P_3 = (f_{31} + f_{32}f_{21})\delta P_1, \tag{B.28}$$

which gives for the first line of (B.18)

$$\delta H_1 = s_{11}\delta P_1 + s_{12}\delta P_2 + s_{13}\delta P_3, \tag{B.29}$$

$$\delta H_1 = s_{11}\delta P_1 + s_{12}f_{21}\delta P_1 + s_{13}(f_{31} + f_{32}f_{21})\delta P_1, \tag{B.30}$$

$$\delta H_1 = (s_{11} + s_{12}f_{21} + s_{13}(f_{31} + f_{32}f_{21}))\delta P_1. \tag{B.31}$$

Here we use

$$\delta H_1 = \frac{1}{E_1}\delta P_1 \tag{B.32}$$

to determine the Young's modulus.

In order to derive the Poisson's ratio, we need to consider the last equation of (B.18) and insert all previous results:

$$\delta H_4 = s_{41}\delta P_1 + s_{42}\delta P_2 + s_{43}\delta P_3, \tag{B.33}$$

$$\delta H_4 = (s_{41} + s_{42}f_{21} + s_{43}(f_{31} + f_{32}f_{21}))\delta P_1, \tag{B.34}$$

$$\delta H_4 = \frac{s_{41} + s_{42}f_{21} + s_{43}(f_{31} + f_{32}f_{21})}{s_{11} + s_{12}f_{21} + s_{13}(f_{31} + f_{32}f_{21})}\delta H_1. \tag{B.35}$$

Again we use the relationship

$$\delta H_4 = -\nu_{14}\delta H_1 \tag{B.36}$$

to determine the Poisson's ratio. Other properties are obtained again in a similar fashion by exchanging the indices.

For the derivation of the linearized modulus of constrained motion in one direction, we need a relation between δP_i and δH_i from

$$\begin{bmatrix} \delta H_1 \\ 0 \\ 0 \\ 0 \end{bmatrix} = \begin{bmatrix} s_{11} & s_{12} & s_{13} & s_{14} \\ s_{21} & s_{22} & s_{23} & s_{24} \\ s_{31} & s_{32} & s_{33} & s_{34} \\ s_{41} & s_{42} & s_{43} & s_{44} \end{bmatrix} \begin{bmatrix} \delta P_1 \\ \delta P_2 \\ \delta P_3 \\ \delta P_4 \end{bmatrix}. \tag{B.37}$$

Using the last line of (B.37), we get

$$0 = s_{41}\delta P_1 + s_{42}\delta P_2 + s_{43}\delta P_3 + s_{44}\delta P_4, \tag{B.38}$$

$$\delta P_4 = -\frac{s_{41}}{s_{44}}\delta P_1 - \frac{s_{42}}{s_{44}}\delta P_2 - \frac{s_{43}}{s_{44}}\delta P_3, \tag{B.39}$$

$$\delta P_4 = f_{41}\delta P_1 + f_{42}\delta P_2 + f_{43}\delta P_3. \tag{B.40}$$

Now putting (B.40) into the third line of (B.37) results in

$$0 = s_{31}\delta P_1 + s_{32}\delta P_2 + s_{33}\delta P_3 + s_{34}\delta P_4, \tag{B.41}$$

$$0 = s_{31}\delta P_1 + s_{32}\delta P_2 + s_{33}\delta P_3 + s_{34}(f_{41}\delta P_1 + f_{42}\delta P_2 + f_{43}\delta P_3), \tag{B.42}$$

$$(s_{33} + s_{34}f_{43})\delta P_3 = (-s_{31} - s_{34}f_{41})\delta P_1 + (-s_{32} - s_{34}f_{42})\delta P_2, \tag{B.43}$$

$$\delta P_3 = \frac{-s_{31} - s_{34}f_{41}}{s_{33} + s_{34}f_{43}}\delta P_1 + \frac{-s_{32} - s_{34}f_{42}}{s_{33} + s_{34}f_{43}}\delta P_2, \tag{B.44}$$

$$\delta P_3 = f_{31}\delta P_1 + f_{32}\delta P_2. \tag{B.45}$$

Inserting this back into (B.40) gives

$$\delta P_4 = f_{41}\delta P_1 + f_{42}\delta P_2 + f_{43}(f_{31}\delta P_1 + f_{32}\delta P_2), \tag{B.46}$$

$$\delta P_4 = (f_{41} + f_{43}f_{31})\delta P_1 + (f_{42} + f_{43}f_{32})\delta P_2. \tag{B.47}$$

Now (B.45) and (B.47) can be inserted into the second row of (B.37) giving:

$$0 = s_{21}\delta P_1 + s_{22}\delta P_2 + s_{23}\delta P_3 + s_{24}\delta P_4, \tag{B.48}$$

$$0 = s_{21}\delta P_1 + s_{22}\delta P_2 + s_{23}(f_{31}\delta P_1 + f_{32}\delta P_2) + s_{24}((f_{41} + f_{43}f_{31})\delta P_1 + (f_{42} + f_{43}f_{32})\delta P_2), \tag{B.49}$$

$$(s_{22} + s_{23}f_{32} + s_{24}(f_{42} + f_{43}f_{32}))\delta P_2 = (-s_{21} - s_{23}f_{31} - s_{24}(f_{41} + f_{43}f_{31}))\delta P_1, \tag{B.50}$$

$$\delta P_2 = \frac{-s_{21} - s_{23}f_{31} - s_{24}(f_{41} + f_{43}f_{31})}{s_{22} + s_{23}f_{32} + s_{24}(f_{42} + f_{43}f_{32})}\delta P_1, \tag{B.51}$$

$$\delta P_2 = f_{21}\delta P_1. \tag{B.52}$$

Again this can be inserted back into (B.45) and (B.47):

$$\delta P_3 = (f_{31} + f_{32}f_{21})\delta P_1, \tag{B.53}$$

$$\delta P_4 = (f_{41} + f_{43}f_{31} + (f_{42} + f_{43}f_{32})f_{21})\delta P_1. \tag{B.54}$$

Finally, (B.52), (B.53), and (B.54) are inserted back into (B.37) to give

$$\delta H_1 = (s_{11} + s_{12}f_{21} + s_{13}(f_{31} + f_{32}f_{21}) + s_{14}(f_{41} + f_{43}f_{31} + (f_{42} + f_{43}f_{32})f_{21}))\delta P_1. \tag{B.55}$$

Now by comparing this to

$$\delta H_1 = \frac{1}{M_1}\delta P_1 \tag{B.56}$$

we can calculate the constrained modulus.

The other constrained modulus as well as the shear moduli are obtained in the same fashion.

References

Alomarah, A., Xu, S., Masood, S.H., Ruan, D., 2020. Dynamic performance of auxetic structures: experiments and simulation. Smart Mater. Struct. 29, http://dx.doi.org/10.1088/1361-665X/ab79bb.

Álvarez Elipe, J.C., Díaz Lantada, A., 2012. Comparative study of auxetic geometries by means of computer-aided design and engineering. Smart Mater. Struct. 21, http://dx.doi.org/10.1088/0964-1726/21/10/105004.

Antman, S.S., 2005. Nonlinear problems of elasticity. Appl. Math. Sci. http://dx.doi.org/10.1007/0-387-27649-1.

Argatov, I.I., Guinovart-Díaz, R., Sabina, F.J., 2012. On local indentation and impact compliance of isotropic auxetic materials from the continuum mechanics viewpoint. Internat. J. Engrg. Sci. 54, 42–57. http://dx.doi.org/10.1016/j.ijengsci.2012.01.010.

Bahaloo, H., Li, Y., 2019. Micropolar modeling of auxetic chiral lattices with tunable internal rotation. J. Appl. Mech. 86, http://dx.doi.org/10.1115/1.4042428.

Bohara, R.P., Linforth, S., Nguyen, T., Ghazlan, A., Ngo, T., 2023. Anti-blast and -impact performances of auxetic structures: A review of structures, materials, methods, and fabrications. Eng. Struct. 276, http://dx.doi.org/10.1016/j.engstruct.2022.115377.

Chen, Z., Liu, L., Gao, S., Wu, W., Xiao, D., Li, Y., 2021. Dynamic response of sandwich beam with star-shaped reentrant honeycomb core subjected to local impulsive loading. Thin-Walled Struct. 161, http://dx.doi.org/10.1016/j.tws.2020.107420.

Choi, J.B., Lakes, R.S., 1992. Non-linear properties of metallic cellular materials with a negative Poisson's ratio. J. Mater. Sci. 27, 5375–5381. http://dx.doi.org/10.1007/bf02403846.

Choi, J.B., Lakes, R.S., 1996. Fracture toughness of re-entrant foam materials with a negative Poisson's ratio: experiment and analysis. Int. J. Fract. 80, 73–83. http://dx.doi.org/10.1007/bf00036481.

Crisfield, M.A., Jelenić, G., 1999. Objectivity of strain measures in the geometrically exact three-dimensional beam theory and its finite-element implementation. Proc. R. Soc. Lond. Ser. A Math. Phys. Eng. Sci. 455, 1125–1147. http://dx.doi.org/10.1098/rspa.1999.0352.

Crouch, I.G., 2019. Body armour – new materials, new systems. Def. Technol. 15, 241–253. http://dx.doi.org/10.1016/j.dt.2019.02.002.

Dynaflow Research Group, 2021. Jive. URL https://dynaflow.com/software/jive/.

Eugster, S.R., 2015. Geometric Continuum Mechanics and Induced Beam Theories. In: Lecture Notes in Applied and Computational Mechanics, http://dx.doi.org/10.1007/978-3-319-16495-3.

Evans, K.E., Nkansah, M.A., Hutchinson, I.J., Rogers, S.C., 1991. Molecular network design. Nature 353, 124. http://dx.doi.org/10.1038/353124a0.

Gálvez Díaz-Rubio, F., Fjeldberg, N., Pernas, J., Varas, D., Martín, J., Cendón Franco, D.A., 2021. On the study of the dynamic response in 3d additively manufactured auxetic structures. In: EPJ Web of Conferences 250. http://dx.doi.org/10.1051/epjconf/202125006004.

Gibson, L.J., Ashby, M.F., Schajer, G.S., Robertson, C.I., 1997. The mechanics of two-dimensional cellular materials. Proc. R. Soc. Lond. Ser. A Math. Phys. Eng. Sci. 382, 25–42. http://dx.doi.org/10.1098/rspa.1982.0087.

Jiang, L., Hu, H., 2017. Low-velocity impact response of multilayer orthogonal structural composite with auxetic effect. Compos. Struct. 169, 62–68. http://dx.doi.org/10.1016/j.compstruct.2016.10.018.

Keskar, N.R., Chelikowsky, J.R., 1992. Negative Poisson ratios in crystalline sio2 from first-principles calculations. Nature 358, 222–224. http://dx.doi.org/10.1038/358222a0.

Körner, C., Liebold-Ribeiro, Y., 2015. A systematic approach to identify cellular auxetic materials. Smart Mater. Struct. 24, http://dx.doi.org/10.1088/0964-1726/24/2/025013.

Larsen, U.D., Sigmund, O., Bouwsta, S., 1997. Design and fabrication of compliant micromechanisms and structures with negative Poisson's ratio. J. Microelectromech. Syst. 6, 99–106. http://dx.doi.org/10.1109/84.585787.

Lees, C., Vincent, J.F.V., Hillerton, J.E., 1991. Poisson's ratio in skin. Bio-Med. Mater. Eng. 1, 19–23. http://dx.doi.org/10.3233/bme-1991-1104.

Lim, T.-C., 2015. Auxetic materials and structures. In: Engineering Materials. Springer Singapore, Singapore, http://dx.doi.org/10.1007/978-981-287-275-3.

Mercer, C., Speck, T., Lee, J., Balint, D.S., Thielen, M., 2022. Effects of geometry and boundary constraint on the stiffness and negative Poisson's ratio behaviour of auxetic metamaterials under quasi-static and impact loading. Int. J. Impact Eng. 169, http://dx.doi.org/10.1016/j.ijimpeng.2022.104315.

Milne, W.E., 1926. Numerical integration of ordinary differential equations. Amer. Math. Monthly 33, http://dx.doi.org/10.2307/2299609.

Munthe-Kaas, H.Z., 2015. Lie Group Integrators. Springer Berlin Heidelberg, Berlin, Heidelberg, pp. 787–790. http://dx.doi.org/10.1007/978-3-540-70529-1_122.

Pan, J., Fang, H., Xu, M.C., Wu, Y.F., 2018. Study on the performance of energy absorption structure of bridge piers against vehicle collision. Thin-Walled Struct. 130, 85–100. http://dx.doi.org/10.1016/j.tws.2018.05.008.

Pardini, C., Anselmo, L., 1999. Assessing the risk of orbital debris impact. Space Debris 1, 59–80. http://dx.doi.org/10.1023/a:1010066300520.

Reda, H., Karathanasopoulos, N., Elnady, K., Ganghoffer, J.F., Lakiss, H., 2018. The role of anisotropy on the static and wave propagation characteristics of two-dimensional architectured materials under finite strains. Mater. Des. 147, 134–145. http://dx.doi.org/10.1016/j.matdes.2018.03.039.

Reissner, E., 1981. On finite deformations of space-curved beams. Z. Angew. Math. Phys. 32, 734–744. http://dx.doi.org/10.1007/bf00946983.

Ren, X., Das, R., Tran, P., Ngo, T.D., Xie, Y.M., 2018. Auxetic metamaterials and structures: a review. Smart Mater. Struct. 27, http://dx.doi.org/10.1088/1361-665X/aaa61c.

Saini, D., Shafei, B., 2019. Prediction of extent of damage to metal roof panels under hail impact. Eng. Struct. 187, 362–371. http://dx.doi.org/10.1016/j.engstruct.2019.02.036.

Simo, J.C., 1985. A finite strain beam formulation. the three-dimensional dynamic problem. part i. Comput. Methods Appl. Mech. Engrg. 49, 55–70. http://dx.doi.org/10.1016/0045-7825(85)90050-7.

Simo, J.C., Vu-Quoc, L., 1986. A three-dimensional finite-strain rod model. part ii: Computational aspects. Comput. Methods Appl. Mech. Engrg. 58, 79–116. http://dx.doi.org/10.1016/0045-7825(86)90079-4.

Smith, C.W., Grima, J.N., Evans, K.E., 2000. A novel mechanism for generating auxetic behaviour in reticulated foams: missing rib foam model. Acta Mater. 48, 4349–4356. http://dx.doi.org/10.1016/s1359-6454(00)00269-x.

Tatlıer, M.S., 2022. A comparative analysis of the in-plane energy absorption capacities of auxetic structures. Trans. Can. Soc. Mech. Eng. 46, 216–224. http://dx.doi.org/10.1139/tcsme-2021-0112.

Wang, Z., Luan, C., Liao, G., Liu, J., Yao, X., Fu, J., 2020. Progress in auxetic mechanical metamaterials: Structures, characteristics, manufacturing methods, and applications. Adv. Eng. Mater. 22, http://dx.doi.org/10.1002/adem.202000312.

Zhang, J., Lu, G., You, Z., 2020. Large deformation and energy absorption of additively manufactured auxetic materials and structures: A review. Composites B 201, http://dx.doi.org/10.1016/j.compositesb.2020.108340.

Zhao, X., Gao, Q., Wang, L., Yu, Q., Ma, Z.D., 2018. Dynamic crushing of double-arrowed auxetic structure under impact loading. Mater. Des. 160, 527–537. http://dx.doi.org/10.1016/j.matdes.2018.09.041.